Investigation of smectite hydration properties by modeling experimental X-ray diffraction patterns. Part I. Montmorillonite hydration properties.

Eric Ferrage, Bruno Lanson, Boris A. Sakharov, Victor A. Drits

Investigation of smectite hydration properties by modeling experimental X-ray diffraction patterns. Part I. Montmorillonite hydration properties

Revision 1

Eric Ferrage[1,2], Bruno Lanson[1], Boris A. Sakharov[3], and Victor A. Drits[3]

[1] Environmental Geochemistry Group, LGIT – Maison des Géosciences, Joseph Fourier University – CNRS, BP53, 38041 Grenoble cedex 9, France

[2] ANDRA, Parc de la Croix Blanche, 1-7 rue Jean Monnet, 92298 Châtenay-Malabry cedex, France

[3] Geological Institute, Russian Academy of Sciences, 7 Pyzhevsky street, 109017 Moscow, Russia

Corresponding author: Eric.Ferrage@obs.ujf-grenoble.fr

ABSTRACT

Hydration of the <1 µm size fraction of SWy-1 source clay (low-charge montmorillonite) was studied by modeling of X-ray diffraction (XRD) patterns recorded under controlled relative humidity (RH) conditions on Li-, Na-, K-, Mg-, Ca-, and Sr-saturated specimens. The quantitative description of smectite hydration, based on the relative proportions of different layer types derived from the fitting of experimental XRD patterns, was consistent with previous reports of smectite hydration. However, the coexistence of smectite layer types exhibiting contrasting hydration states was systematically observed, and heterogeneity rather than homogeneity seems to be the rule for smectite hydration. This heterogeneity can be characterized qualitatively using the standard deviation of the departure

from rationality of the 00ℓ reflection series (ξ), which is systematically larger than 0.4 Å when the prevailing layer type accounts for ~70% or less of the total layers (~25 of XRD patterns examined). In addition, hydration heterogeneities are not randomly distributed within smectite crystallites, and models describing these complex structures involve two distinct contributions, each containing different layer types that are randomly interstratifed. As a result, the different layer types are partially segregated in the sample. However, these two contributions do not imply the actual presence of two populations of particles in the sample.

XRD profile modeling has allowed also the refinement of structural parameters, such as the location of interlayer species and the layer thickness corresponding to the different layer types, for all interlayer cations and RH values. From the observed dependence of the latter parameter on the cation ionic potential ($\frac{v}{r}$, v = cation valency and r = ionic radius) and on RH, the following equations were derived:

$$\text{Layer thickness (1W)} = 12.556 + 0.3525 \times \left(\frac{v}{r} - 0.241\right) \times (v \times RH - 0.979)$$

$$\text{Layer thickness (2W)} = 15.592 + 0.6472 \times \left(\frac{v}{r} - 0.839\right) \times (v \times RH - 1.412)$$

which allow the quantification of the increase of layer thickness with increasing RH for both 1W (one-water) and 2W (two-water) layers. In addition for 2W layers interlayer H_2O molecules are probably distributed as a unique plane on each side of the central interlayer cation. This plane of H_2O molecules is located at ~1.20 Å from the central interlayer cation along the *c** axis.

INTRODUCTION

Bentonite has been long used as buffer material for engineered barriers in municipal waste disposal sites because of its low permeability when compacted and because of its cation-retention ability. These properties also make bentonite a possible buffer material in multi-barrier designs for nuclear waste repositories. Specifically, bentonite may be used to isolate intermediate-level long-lived wastes (ILLW wastes) from the geological barrier, and from the biosphere. The retention and mechanical properties of this material are mainly influenced by its smectite component. The high smectite content provides bentonite with a self-healing capacity and the ability to sorb cations, the latter being enhanced by the high surface area of smectite. Sorption would help limit and/or delay possible radionuclide migration. Both properties result from the specific hydration/expansion ability of this mineral component.

However, interactions between the nuclear waste package and the bentonite barrier could possibly alter these properties. For example, concrete as a civil engineering material or as a component of the waste package will produce alkali-rich high pH aqueous solutions ("pH plume") during alteration. The effect of such solutions on smectite has been widely studied (Mohnot et al. 1987; Carroll-Webb and Walther 1988; Carroll and Walther 1990; Chermak 1992, 1993; Eberl et al. 1993; Huang 1993; Bauer and Berger 1998; Bauer et al. 1998; Bauer and Velde 1999; Cama et al. 2000; Taubald et al. 2000; Huertas et al. 2001; Rassineux et al. 2001; Claret et al. 2002). Smectite in the bentonite can be affected also by a thermal pulse resulting from the radioactivity of the waste package. By analogy with burial diagenesis in sediments (Weaver 1960; Hower and Mowatt 1966; Burst 1969; Perry and Hower 1972; Hower et al. 1976, etc.) smectite is expected to transform with increasing temperature into non-expandable illite through intermediate mixed-layer structures. Structural changes of

smectites during the early stages of this transformation relate to the location and the amount of layer charge (Sato et al. 1996; Drits et al. 1997a; Beaufort et al. 2001). Because these changes probably produce subtle changes of the hydration/expansion properties of the smectite, which persist throughout subsequent stages of the illitization reaction (Drits et al. 1997a), a careful study of these hydration properties using X-ray diffraction (XRD) is possibly a way to investigate the early steps of the smectite-to-illite transition. However, because these properties also vary as a function of the nature of the interlayer cation and of relative humidity, the influence of these two parameters must be assessed first for reference smectite samples. In addition, the intrinsic heterogeneity of smectite materials (Calarge et al. 2003; Meunier et al. 2004) can lead to the coexistence within the same crystallite of layers exhibiting different hydration states. This effect can be quantified by comparing XRD patterns recorded under stable experimental conditions with patterns calculated assuming a random interstratification of layers exhibiting different hydration states.

This paper reports on a detailed characterization of the hydration properties of a low-charged montmorillonite reference sample (the Clay Mineral Society source clay, SWy-1). Following purification and size fractionation, aliquots of the <1-µm size fraction of this reference sample were saturated with K^+, Na^+, Li^+, Sr^{2+}, Ca^{2+} and Mg^{2+} interlayer cations. Experimental XRD patterns were recorded at fixed relative humidity (RH) conditions over a range from an essentially dry atmosphere (~0% RH) to approximately 80% RH. Experimental XRD patterns were compared to calculated models for each cation and each relative humidity to obtain the proportion of layers with defined hydration states. Additional structural parameters, such as the thickness of hydrated layers, the distribution of interlayer H_2O molecules were also assessed with this modeling approach.

BACKGROUND

The ability of some 2:1 phyllosilicates, including smectites, to incorporate interlayer H_2O molecules and the subsequent change in basal spacing has been extensively studied for several decades. For example, Nagelschmidt (1936) and Bradley et al. (1937) showed by XRD that the basal spacing of smectite increases in steps as the amount of water increases in the sample environment. These discrete steps were later attributed to the intercalation of 0, 1, 2 or 3 planes of H_2O molecules in the smectite interlayer (Mooney et al. 1952; Méring and Glaeser 1954; Norrish 1954; Walker 1956). From these pioneering studies, hydration properties of 2:1 phyllosilicates (smectites) were shown to be controlled by such factors as the type of the interlayer cation, and the amount and the location of layer charge (octahedral or tetrahedral sites). These observations suggested several possible models where crystalline swelling is controlled by the balance between the repulsive force owing to 2:1 layer interactions and the attractive forces between hydrated interlayer cations and the negatively charged surface of siloxane layers (Norrish 1954; Van Olphen 1965; Kittrick 1969a, 1969b; Laird 1996, 1999).

Smectite hydration properties are often characterized by XRD from the evolution of *d*(001) basal-spacing value under variable RH (Méring and Glaeser 1954; Harward and Brindley 1965; Glaeser and Méring 1967, 1968; Harward et al. 1969; Watanabe and Sato 1988; Sato et al. 1992; Yamada et al. 1994; Tamura et al. 2000, among others). Modeling techniques complement this approach. For example, Ben Brahim et al. (1983a, 1983b, 1984) studied the interlayer structure (atomic positions of interlayer cations and associated H_2O molecules) of Na-saturated montmorillonite and beidellite samples.

However, these studies systematically assume homogeneous hydration conditions for a given cation at a given RH whereas the coexistence of different hydration states in a sample

119 is probably common even under controlled conditions (Méring and Glaeser 1954; Glaeser and
120 Méring 1967; Sato et al. 1992, 1996). For example, the irrational character of the $d(00\ell)$
121 reflection series at the transition between two discrete hydration states and the asymmetric
122 profiles of high-angle reflections indicate such coexistence, most likely arising from a
123 heterogeneous layer-charge distribution (Sato et al. 1992). Few studies have taken into
124 account the coexistence of layers with contrasting layer thickness corresponding to different
125 hydration states. Moore and Hower (1986) studied ordered structures composed of mono-
126 hydrated and collapsed interlayers in montmorillonite and Cuadros (1997) estimated the H_2O
127 content of smectite as a function of the interlayer cation. Using a similar approach, Iwasaki
128 and Watanabe (1988) were able to investigate the distribution of Na^+ and Ca^{2+} cations over
129 the interlayers of smectite and smectite-illite mixed-layer structures. Assessing the cationic
130 composition of smectite interlayers from the layer thickness (~15.0 and 12.5 Å for Ca^{2+} and
131 Na^+, respectively) Iwasaki and Watanabe (1988) demonstrated that Na^+ and Ca^{2+} cations
132 occur in different interlayers leading to the presence of segregated domains. These domains
133 are reminiscent of the "demixed state" described in the early works of Glaeser and Méring
134 (1954), Levy and Francis (1975) and Mamy and Gaultier (1979).

135 Bérend et al. (1995) and Cases et al. (1997) applied such a XRD profile modeling
136 approach in combination with adsorption-desorption isotherm experiments to assess the
137 proportion of the different layer types (with 0-3 planes of interlayer H_2O molecules)
138 coexisting along the isotherms. However, their calculations were limited to reproduce the
139 position of the 001 reflection, whereas positions and shapes of higher-order 00ℓ reflections
140 were not considered. These limitations did not allow a complete description of the real
141 structure of their samples. More recently, Calarge et al. (2003) and Meunier et al. 2004)
142 refined this approach by fitting both positions and profiles of the 00ℓ reflections over a large

143 angular range and showed that randomly interstratified structures, each containing different
144 layer types, coexisted in their montmorillonite samples.

145 To our knowledge, no study has described the interlayer structure of smectite as a
146 function of RH for the different layer types, and possibly for different cations. The interlayer
147 structure was determined for 0-3 planes of interlayer H_2O over a limited RH range for which
148 the hydration of smectite is considered to be homogeneous. However, the coexistence of
149 different layer types over an extended RH range has not allowed the interlayer structure to be
150 determined as a function of RH. Furthermore, in most studies of hydration heterogeneity of
151 smectite, the structure of the interlayer H_2O has not been refined because the XRD profile
152 fitting was usually performed over a limited angular range.

153

154 ## MATERIAL AND METHODS

155

156 ### Sample preparation

157 The smectite used for this study is the SWy-1 montmorillonite reference from the
158 Source Clay Repository of The Clay Mineral Society with structural formula (Stucki et al.
159 1984): $[(Al_{2.99}\ Fe_{0.43}\ Mg_{0.52})(Si_{7.97}\ Al_{0.03})O_{20}(OH)_4]\ M^{+}_{0.70}$ (<2-μm size fraction) This
160 montmorillonite is originally Na-saturated, and exhibits a low octahedral charge and
161 extremely limited tetrahedral substitutions (Mermut and Lagaly 2001).

162 Size fractionation was performed by centrifugation to obtain a suspension of the
163 <1 μm size fraction. Each ion exchange was made at room temperature with 1 $mol.L^{-1}$
164 aqueous solutions of K-, Na-, Li-, Ca-, and Sr-chlorides, respectively. SWy-1 suspensions in
165 each saline solution (~50mg of solid in ~50mL of solution) were shaken mechanically for 24h
166 before separation of the solid fraction by centrifugation and addition of fresh saline solution.
167 These steps were repeated three times to ensure a complete cation exchange. Removal of the

168 excess chloride was performed by washing the solid three times by immersion for 24h in
169 distilled water (Milli-Q / 18.2 MΩ cm^{-1}). The Mg-saturated sample was obtained using a
170 0.5mol.L^{-1} solution of magnesium perchlorate to ensure the complete dissociation of the
171 $Mg(ClO_4)_2$ complex in water. Ten steps consisting of a 24h contact between the solution and
172 the solid followed by centrifugation and renewal of the saline solution guaranteed the
173 complete saturation before the three steps of washing. These samples are hereafter referred to
174 as K-, Na-, Li-, Sr-, Ca-, and Mg-SWy-1.
175
176 **X-ray diffraction**
177 Oriented slides were prepared for each sample by drying at room temperature a
178 pipetted clay slurry covering a glass slide. XRD patterns were then recorded using a Siemens
179 (Bruker) D5000 diffractometer using Cu Kα radiation and equipped with an Ansyco rh-plus
180 2250 humidity control device coupled to an Anton Paar TTK450 chamber. Usual scanning
181 parameters were 0.04°2θ as step size and 6s as counting time per step over the 2-50°2θ
182 angular range. The divergence slit, the two Soller slits, the antiscatter and resolution slits were
183 0.5°, 2.3°, 2.3°, 0.5° and 0.06°, respectively. The relative humidity range used in the present
184 study extends from almost saturated conditions (80% RH) to extremely dry conditions (~0%
185 RH), the latter being obtained by evacuating the entire Paar chamber to a secondary vacuum
186 (~10^{-4} Pa). For all samples, XRD patterns were first recorded under room conditions (297 K,
187 and ~35% RH), which were controlled (RH) or monitored (temperature) and found stable
188 over the entire data collection period. Then, XRD patterns were recorded for all samples
189 following the same sequence of RHs (40, 60, 80%, 20% and 0%) to avoid a possible
190 irreversible collapse of some layers at low RH values. For any given sample, all six
191 experimental XRD patterns were recorded within a timeframe that did not exceed 48 hours

192 after the drying of the oriented preparation. This procedure avoided any kinetically driven
193 dehydration process to occur.

194 The algorithms developed initially by Drits and Sakharov (1976) and more recently
195 by Drits et al. (1997a) and Sakharov et al. (1999) were used to fit experimental XRD profiles
196 over the 2-50°2θ range using a trial-and-error approach. Instrumental and experimental
197 factors such as horizontal and vertical beam divergences, goniometer radius, length and
198 thickness of the oriented slides were measured and introduced without further adjustment.
199 The mass absorption coefficient (μ^*) was set to 45, as recommended by Moore and Reynolds
200 (1997, p. 361), whereas the parameter characterizing the preferred orientation of the sample
201 (σ^*) was considered as a variable parameter as discussed below. The *z* coordinates for all
202 atomic positions within the 2:1 layer framework were set as proposed by Moore and Reynolds
203 (1997, p. 368), but *z* coordinates of interlayer species were further refined to improve the
204 quality of fit. Additional variable parameters include the coherent scattering domain size
205 (CSDS) along the *c** axis which was characterized by a maximum CSDS, set to 45 layers, and
206 by a variable mean CSDS value (N, Drits et al. 1997b). In addition, because of the weak
207 bonding between adjacent smectite layers, the layer spacing likely deviates from its average
208 *d*(001) value. This cumulative deviation from periodicity was described as "disorder of the
209 second type" by Guinier (1964) and detailed later by Drits and Tchoubar (1990) and (Drits et
210 al. (2005), and can be considered as crystal strain. A variance parameter σ_z was introduced to
211 account for this strain. The effect of σ_z on the profiles of calculated XRD patterns is
212 illustrated in Figure 1 for Ca-SWy-1 exhibiting a homogeneous hydration state with a layer
213 thickness of 15.10 Å. When σ_z increases from zero (which corresponds to an ideal periodic
214 structure) to 0.3 Å, the resulting high-angle maxima are significantly broadened. Moreover,
215 their relative intensity is decreased as compared to low-angle reflections that are basically

unaffected (Fig. 1). The overall fit quality was assessed using the unweighted R_p parameter (Howard and Preston 1989):

$$R_p = \sqrt{\frac{\sum[I_{obs}(2\theta_i) - I_{calc}(2\theta_i)]^2}{\sum I_{obs}(2\theta_i)^2}} \quad \text{Equation 1}$$

where I_{obs} and I_{calc} represent measured and calculated intensities, respectively, at position $2\theta_i$, the subscript i running over all points in the refined angular range. This parameter is mainly influenced by the most intense diffraction maxima, such as the 001 reflection, which contains essential information on the proportions of the different layer types and on their layer thickness.

Fitting strategy

XRD-pattern modeling was performed assuming the possible presence of different layer types. These different layer types correspond to the different hydration states commonly reported in smectites as a function of relative humidity. In the fitting process, we have introduced dehydrated layers (0W layers, layer thickness at 9.6-10.1 Å), mono-hydrated layers with one plane of H_2O molecules in the interlayer (1W layers at 12.3-12.7 Å), and bi-hydrated layers with two planes of H_2O molecules in the interlayer (2W layers at 15.1-15.8 Å). Because we did not consider RH values greater than 80%, no evidence for tri-hydrated layers (3W layers at 18.0-18.5 Å) was observed. If a good fit was not obtained with a unique periodic structure corresponding to one of the layer types, it was first assumed that this contribution is related to a randomly interstratified mixed-layer structure containing different layer types. If necessary, additional contributions, each containing different layer types in variable proportions, were introduced to reproduce the experimental XRD pattern. However, the use of two mixed-layer structures to fit all features of experimental XRD patterns does not imply the actual presence of two populations of particles in the sample as

240 discussed below. As a consequence, layers in the same hydration state that are present in the
241 different mixed-layer structures must have identical properties at a given RH value. Each
242 given layer type was thus assigned a unique chemical composition, a unique layer thickness
243 value, and a unique set of atomic coordinates for all mixed-layer structures at a given RH.
244 Similarly, identical values of σ^*, N and σ_z parameters were used for all mixed-layer structures
245 at a given RH. Each parameter was allowed to vary as a function of relative humidity. The
246 relative proportions of each mixed-layer structure and of each layer type in these structures
247 were varied to fit experimental XRD patterns. Following Bérend et al. (1995) and Cases et al.
248 (1997), the strategy used for XRD profile modeling was to match closely the 001 reflection of
249 SWy-1 using a mixed-layer structure as homogeneous as possible, i.e., containing as few
250 different layer types as possible. If necessary to obtain a good fit, a second mixed-layer
251 structure was introduced to better match the calculated and experimental patterns, and to
252 better account for the hydration heterogeneity of the sample. This strategy is illustrated in
253 Figure 2 using the XRD pattern obtained for K-SWy-1 at 0% RH (Fig. 2).

254 The pattern exhibits four major diffraction maxima with positions that do not deviate
255 much from those expected for a rational series. However, significant asymmetry is observed
256 on the low-angle side of the first maximum and on the high-angle side of the third maximum.
257 The second maximum exhibits significant tail broadening (arrows on Fig. 2a). The difference
258 plot between the experimental pattern and that calculated for dehydrated smectite (100% of
259 0W layers) shows maxima corresponding to the features mentioned above (Fig. 2b). It was
260 not possible to reproduce these specific features with a single contribution corresponding to a
261 mixed-layer structure. Rather, comparison between the positions of the maxima present on
262 this difference plot with those corresponding to 0W (light gray ticks) and to 1W (dark gray
263 ticks) smectite and the use of Méring's principle (Méring 1949) suggest that they are probably
264 related to a mixed-layer structure containing these two layer types. This result arises from

coincidence between the features of the difference plot and the arrows. This depiction shows the position and breadth of the diffraction maxima of a mixed-layer structure as expected from Méring's principle (Fig. 2b). Two structures thus appear to be present: the initial structure (S1, 100% 0W layers) and a second (S2). The latter results from the random interstratification of 0W and 1W layers (70% and 30%, respectively). A good fit (Rp = 3.73%) is obtained assuming a 81:19 ratio between S1 and S2 (Fig. 2c). A schematic of this result is given in Figure 2d where the relative proportions of the two structures contributing to the diffraction intensity are illustrated along the vertical axis by their respective surface areas in the square box whereas the proportion of the different layer types in each mixed-layer structure is represented on the horizontal axis.

Note that calculated XRD patterns are not plotted in the low-angle region (2θ angles lower than 7° in the present case) because the computed "background" shape in this region is not compatible with that measured on experimental patterns. The origin of this discrepancy is discussed below.

RESULTS

Qualitative description of experimental patterns

Figure 3 shows the evolution as a function of RH of the $d(001)$ values measured on the experimental XRD patterns. These values are also listed in Table 1 together with the full width at half maximum intensity (FWHM) of the 001 reflection. Table 1 also includes the standard deviation of the departure from rationality (ξ) of the 00ℓ reflection series. This latter parameter is calculated as the standard deviation of the $\ell \times d(00\ell)$ values calculated for all measurable reflections over the 2θ = 2-50° range. On Figure 3, the usual hydration states are observed for smectites with 0W layers ($d(001)$ at 9.6-10.1 Å) observed only at 0% RH for

290 Na-, K-, and Sr-SWy-1, 1W layers (d(001) at 12.3-12.7 Å), 2W layers (d(001) at 15.0-15.8 Å)
291 as given by Sato et al. (1992). However, the common coexistence of different hydration states
292 are identified both from a $d(00\ell)$ value intermediate between those corresponding to the usual
293 discrete hydration states (gray domains in Fig. 3) and from a high ξ value indicating the
294 irrationality of 00ℓ reflections (open symbols in Fig. 3). K-SWy-1, for example, shows mostly
295 coexisting hydration states in Figure 3. The heterogeneity of hydration states, which leads to
296 the interstratification of different layer types, produces an increased FWHM of the diffraction
297 maxima as illustrated in Figure 4 which shows the correlation between the ξ parameter and
298 the FWHM measured on the 001 reflection. From Figures 3 and 4, maximum values can be
299 defined for both the FWHM of the 001 reflection ($2\theta = 1.1°$) and the ξ parameter (0.4 Å)
300 limiting the "homogeneous" hydration domains. Values higher than these limits correspond to
301 an extremely heterogeneous hydration state and/or to the transition between two discrete
302 hydration states.
303 However, within these "homogeneous" or "heterogeneous" hydration domains
304 additional structural features can be determined from the careful examination of experimental
305 XRD patterns (Fig. 5). In particular, within homogeneous 2W domains (Na-SWy-1 and Li-
306 SWy-1: 80% RH, Sr-SWy-1: 40-80% RH, Ca-SWy-1: 35-80% RH and Mg-SWy-1: 20-80%
307 RH) the position and the width (FWHM) of the 001 reflection vary as a function of RH
308 together with the ξ parameter (Table 1). Specifically, for samples saturated with divalent
309 cations the d(001) value increases with increasing RH whereas both the FWHM of the 001
310 reflection and the ξ parameter decrease. On experimental XRD patterns, the 002 reflection
311 appears as a sharp and well-defined reflection only when the values of the latter two
312 parameters are minimized (Sr-SWy-1: 60-80% RH, Ca-SWy-1: 80% RH and Mg-SWy-1: 60-
313 80% RH, Figs. 5d, 5e, 5f). The position of the 001 reflection also varies as a function of RH
314 within homogeneous 1W hydration state (Na-SWy-1: 35-60% RH, Li-SWy-1: 20-60% RH,

315 and Sr-SWy-1: 20-35% RH) whereas other qualitative parameters remain constant for a given
316 sample (Table 1). A homogeneous dehydrated state is observed only under vacuum conditions
317 (0% RH) for K-SWy-1 , Na-SWy-1 and Sr-SWy-1 samples. The experimental XRD patterns
318 of these three samples exhibit well-defined sharp 00ℓ reflections (Figs. 5a, 5b, 5d).

319 In contrast, the presence of important hydration heterogeneities induce specific
320 features on experimental XRD patterns (K-SWy-1: 20-80% RH, Na-SWy-1: 20% RH, Li-
321 SWy-1 and Mg-SWy-1: 0% RH, and Ca-SWy-1: 0-20% RH). For example, XRD patterns of
322 K-SWy-1 over the 20-80% RH range show well-defined reflections only at 11.0-12.0 Å and
323 ~3.25 Å (Fig. 5a). Other reflections appear as broad and diffuse maxima. The sharpness of the
324 ~3.25 Å maximum is related to the proximity between the 003 reflection of dehydrated
325 smectite (~3.3 Å) and the 004 reflection of the mono-hydrated smectite (~3.1 Å). In addition,
326 note that for higher RH values (40-80% RH) the FWHM of the 001 reflection is at a
327 maximum although its position is close to the usual position for 1W layers. This result may be
328 related to the increasing proportion of 2W layers, or to the residual presence of a high
329 proportion of 0W layers. In the latter case, the shift in position of the 001 reflection induced
330 by a relatively large proportion of 0W layers is limited because the structure factor of 0W
331 layers is much smaller than that of 1W layers over the considered angular range, whereas the
332 interstratification leads to increased FWHM values (Drits et al. 1994). If the heterogeneity is
333 produced by the presence of 2W layers, the diffraction maximum at ~3.25 Å remains mostly
334 unaffected as interferences with the 005 reflection of a 2W smectite (at ~3.10 Å) would not
335 cause broadening. For Na-SWy-1 recorded at 20% RH, the measured irrationality of the 00ℓ
336 reflection positions is associated, as for K-SWy-1, with a significant broadening of all
337 diffraction maxima except for the two reflections at ~12.0 Å and ~3.10 Å, which remain sharp
338 and well defined (Fig. 5b). For Li-SWy-1 at 0% RH, note that even the maximum at ~3.10 Å
339 is significantly broadened (Fig. 5c). For Ca-SWy-1 at 0% RH, the position of the 001

reflection at ~11.7 Å is shifted away from values expected for a 1W smectite. In addition there is a significant broadening of this reflection ($2\theta = 1.12°$, Table 1). Accordingly, the ξ parameter is relatively large (0.50 Å, Table 1) and the reflection at ~2.95 Å is poorly defined, which occurs only when heterogeneous hydration states coexist within the sample. Similar observations can be made on the XRD pattern recorded for Mg-SWy-1 at 0% RH (Fig. 5f). For Ca-SWy-1 at 20% RH, the ~3.1 Å peak is even more diffuse, in agreement with the large values of the FWHM of the 001 reflection and of the ξ parameter ($2\theta = 1.24°$ and 0.93 Å, respectively, Table 1).

Qualitative descriptions such as those above have allowed the determination of the main hydration states of smectites by using the position of the 001 reflection, and the characterization of smectite hydration properties as a function of the magnitude and location of layer charge (Harward and Brindley 1965; Harward et al. 1969; Yamada et al. 1994; Tamura et al. 2000). Parameters such as FWHM of the 001 reflection, or the irrational character of 00ℓ reflections provide additional data on the hydration state of these minerals and especially on their hydration heterogeneity (Watanabe and Sato 1988; Sato et al. 1992). However, results described above indicate that although the general descriptions are similar for all parameters, specific features of the XRD patterns, such as the resolution of the 002 reflection for 2W smectite (e.g.), are not accounted for by parametric descriptions. Furthermore, although these parameters allow the assessment of coexisting smectites layers with different hydration states in the same sample, they do not provide detailed insight into this heterogeneity. To achieve this goal, and in particular to determine quantitatively the relative proportions of the different layer types and their structural characteristics (e.g., layer thickness and number of interlayer H_2O molecules) the experimental XRD patterns were modeled using a trial-and-error approach described by Drits and Tchoubar (1990).

365 **Modeling of X-ray diffraction profiles**

366 XRD patterns were fitted using the strategy described above. Structural models to
367 obtain optimum fits shown in Figure 5 are described schematically (relative proportion and
368 composition of the different mixed-layer structure contributions) in Figure 6. The relative
369 proportions of the different layer types are reported in Figure 7 as a function of RH, whereas
370 structural parameters are listed in Table 2.

371 **K-SWy-1 sample.** At 0% RH, the optimum model (described in the Methods
372 section) is consistent with the qualitative description of the sample with a major contribution
373 from a pure 0W smectite and a minor contribution from a mixed-layer structure containing
374 0W and 1W layers in a 70:30 ratio (Fig. 6a). The latter mixed-layer structure accounts for the
375 low-angle asymmetry of the 001 reflection and for the tail broadening of the 002 reflection.
376 Layer thickness of both 0W and 1W layers (10.0, and 12.4 Å, respectively) are consistent
377 with published values. The broadening of the second-order diffraction maximum with
378 increasing RH (Fig. 5a) is related to the increasing proportion of 1W and 2W layers for each
379 of the two mixed-layer structure contributions (Fig. 6a). The two mixed-layer structures also
380 account for the increase of the ξ parameter with increasing RH (Table 1). The increased
381 proportion of 1W layers with increasing RH produces a shift of the ~3.25 Å diffraction
382 maximum toward higher angles. However, 0W layers are still prevailing at 80% RH, although
383 the sample was not totally dehydrated before collecting this XRD pattern. At this high RH
384 value, the position of the 001 reflection (12.04 Å, Table 1) differs significantly from the value
385 expected for 0W smectite, because of the contrasting structure factors of 0W and 1W layer
386 types (Drits et al. 1994). The large FWHM value measured for the 001 reflection results likely
387 from the combination of the large number of 0W layers and of the minor presence of 2W
388 layers. Structural parameters leading to the optimal fits (Fig. 5a) such as σ^*, N and σ_z do not

389 vary significantly as a function of RH (4-5°, 8-13 layers and 0.20-0.25 Å, respectively, Table
390 2).

391 **Na-SWy-1 sample.** In agreement with its qualitative description, and with the
392 presence of sharp and well-defined diffraction maxima, this sample contained a large
393 proportion of 0W, 1W, and 2W layers at 0%, 35-60, and 80% RH, respectively. At these
394 different RHs, the main layer type was essentially present in a major mixed-layer structure
395 exhibiting little, if any, hydration heterogeneity. A minor mixed-layer structure accounts for
396 most of the hydration heterogeneity. At 0% RH, this minor mixed-layer structure produces
397 low-angle asymmetry of the 001 reflection and tail broadening of the 002 reflection. From 35-
398 60% RH, the minor mixed-layer structure accounts for the low-angle asymmetry of the 001
399 reflection (at ~12.4 Å) and for the broad hump on the high-angle side of the 002 reflection. At
400 80% RH, the minor mixed-layer structure contributes on the high-angle side of the 001
401 reflection (~15.3 Å) and also accounts for the slight asymmetries of 003 and 005 reflection
402 (~5.2 and ~3.1 Å, respectively).

403 As expected from the high values measured for both the FWHM of the 001 reflection
404 and the ξ parameter (Table 1), hydration of this sample is more heterogeneous at 20% RH. In
405 this case, two mixed-layer structures are present in similar proportions, and they both include
406 at least two layer types in significant proportions. As a result, 1W and 0W layers, which
407 prevail in this intermediate hydration state, account for 63 and 33% of all layers, respectively
408 (Figs. 6b, 7b). The two mixed-layer structures contributions describing this experimental
409 XRD pattern give similar contributions to the diffracted intensity. However, the small
410 composition difference between the two mixed-layer structures allows for a better fit to the
411 broadened and diffuse maxima.

412 As a result of experimental constraints, XRD patterns of Na-SWy-1 were collected
413 from two oriented slides. One was used for the 0% and 20% RH measurements, whereas the

414 other covered the 35-80% RH range. This difference is especially visible on the σ* value (5-
415 6°, and ~3° for the 0-20 and 35-80% RH ranges, respectively, Table 2), and possibly on the σ_z
416 parameter. Despite this experimental hiatus, values obtained for all other structural parameters
417 are consistent throughout the range of RH (Table 2).

418 **Li-SWy-1 sample.** In agreement with the low values of the FWHM of the 001
419 reflection and of the ξ parameter (Table 1), XRD patterns recorded for Li-SWy-1 at 20-60%
420 RH can be satisfactorily reproduced with a main homogeneous 1W smectite and the accessory
421 contribution of a mixed-layer structure containing all three layer types (Figs. 5c, 6c). The
422 mixed-layer structure accounts for the slight asymmetry of the 001 reflection and for the
423 broad hump on the high-angle side of the 002 reflection. The hump increases with increasing
424 RH from the growing proportion of 2W layers. At 80% RH, 2W layers prevail but each
425 mixed-layer structure includes a significant proportion of 1W layers, and even a few 0W
426 layers (Figs. 6c, 7c). The minor mixed-layer structure contribution allows fitting better the
427 high-angle side of the 001 and 005 peaks, and the low-angle side of the 003 reflection. The
428 maximum hydration heterogeneity occurs at 0% RH, and a satisfactory fit was achieved by
429 using two mixed-layer structures contributions (38:62 ratio), each containing 0W and 1W
430 layers. The main features of these two contributions to the diffracted intensity are similar
431 although shifted in position as a result of the contrasting proportions of the two layer types
432 (30, and 50 % of 0W layers respectively). The combination of these similar features and of
433 their positional shift allowed reproducing the broad and diffuse diffraction maxima obtained
434 for the second and third order reflections.

435 **Sr-SWy-1 sample.** The sharp and well-defined maxima observed on all XRD
436 patterns for Sr-SWy-1 were modeled assuming a major homogenous contribution (Figs. 5d,
437 6d). For example, a homogeneous 2W smectite represents the main contribution over the 60-
438 80% RH range. In addition to this homogeneous phase, a minor mixed-layer structure,

incorporating all three layer types accounts for the broadened tails of all reflections and for the high-angle side asymmetry of the 001 reflection. At 40% RH, hydration heterogeneity occurs as expected from the increased ξ parameter (0.14 Å as compared to 0.06 Å for the 60-80% RH range, Table 1). For this RH value, 2W layers prevail at ~75% of all smectite layers (Fig. 7d), but 0W and 1W layers coexist in the two mixed-layer structures contributing to the calculated pattern. The contributions of these two mixed-layer structures are quite similar, although their slight positional shift allows reproducing the faint asymmetry and broadening of the different reflections. From 40 to 80% RH, the intensity of the ~3.1 Å diffraction maximum decreases whereas the 002 reflection becomes sharper and better defined. The latter evolution of the peak profiles and intensity is related to the decreasing amount of 1W layers when 2W layers prevail (Fig. 7d). The decreased intensity of the ~3.1 Å diffraction maximum results from the increase of layer thickness for 2W layers which induces in turn a decrease of the structure factor.

A RH only 5% lower induces a dramatic hydration change as 1W layers are prevailing at 35% RH. A pure 1W smectite accounts for about half of the diffracted intensity. 1W layers are also prevailing in the complementary mixed-layer structure. The latter contribution accounts for the low-angle side asymmetry of the 001 and 004 reflections and for the high-angle side tail of the 002 reflection. A similar structure model was used to fit the XRD pattern of Sr-SWy-1 recorded at 20% RH although the mixed-layer structure accounts for about 60% of the diffracted intensity. The relative contribution of the pure 1W smectite is decreased. Finally, at 0% RH a unique mixed-layer structure dominated by 0W layers (80% of the layers) randomly interstratified with 1W layers was considered (Fig. 6d). Note on this experimental XRD pattern the presence of a broad reflection on the low-angle side of the 001 reflection. This reflection at ~22 Å could possibly correspond to a regular (R = 1 with maximum possible degree of order) mixed-layer structure containing similar proportions of

0W and 1W layers. However, all attempts to include this contribution to the overall fit proved unsuccessful, most likely because of intrinsic problems in fitting the low-angle region (see the Discussion section).

Ca-SWy-1 sample. XRD patterns recorded for the Ca-SWy-1 sample over the 35-80% RH range were all fitted assuming the coexistence of two mixed-layer structures with very consistent compositions (Figs. 5e, 6e). The most homogeneous one accounts for ~40% of the diffracted intensity and contains essentially 2W layers and a few 1W layers whereas the main mixed-layer structure contains the three layer types. The latter contribution accounts for the high-angle asymmetry of the 001 reflection, for the broadened tails of the 003 reflection and for the shift toward lower-angles of the 005 peak. All these features are reduced with increasing RH as the content of 0W and 1W layers decreases. However, the 002 reflection is systematically broad as an indication of the significant proportion of 0W and 1W layers in the structure, in contrast to the Sr-SWy-1 patterns at high RH values.

For lower RH values, smectite hydration is more heterogeneous, and the ~3.1 Å diffraction maximum is diffuse (Fig. 5e). At 0% RH, heterogeneity was described as resulting from the coexistence of two mixed-layer structures with similar compositions. 1W layers are prevailing in the two structures despite the essentially dry atmosphere. Differences in the composition of these two mixed-layer structures were necessary for fitting the broadened tails of the 00ℓ reflections. At 20% RH, even though both mixed-layer structures contain the three layer types their respective contributions to the diffracted intensity are more contrasted, one being dominated by 1W layers whereas 2W layers prevail in the other one (Fig. 6e). These two mixed-layer structures equally contribute to the diffracted intensity to fit in particular the tabular shape of the complex diffraction maximum at ~3.1 Å (Fig. 5e). Both the similar intensity of these two contributions and their internal heterogeneity induce a significant irrationality of 00ℓ reflections (Table 1).

Mg-SWy-1 sample. Over the 20-80% RH range, one of the two mixed-layer structures essentially contains 2W layers (90-95%), and its relative amounts increases from 53-81% with increasing RH (Fig. 6f). A peculiar characteristic of the second mixed-layer structure, in which 2W layers also dominate, is the presence of 0W layers which systematically prevail over 1W layers. As a result, the 002 reflection is systematically diffuse. At 60 and 80% RH, the second contribution accounts for the high-angle asymmetry of the 001 reflection, and for the broadened tails of the 003 and 005 reflections. At lower RH (20-40% RH), experimental XRD patterns are strikingly different from those collected at 60-80% RH even though the structure models are similar (Fig. 6f). This is mostly due to the dramatic change in the layer thickness of 2W layers which is decreased to a stable value of 14.2-14.8 Å over the 20-40% RH range. This leads to a significant shift of the 003 and 005 reflections toward higher angles and to the strong increase in intensity of the 004 reflection. This increase results from the variation of the structure factor induced by the layer-thickness modification. These additional features indicate that the positional shift of the 001 reflection actually results from a modification of the layer thickness of 2W layers, rather than from the interstratification of different layer types. This hypothesis is consistent with the values determined for the FWHM of the 001 reflection and for the ξ parameter (0.8-1.0° and 0.2-0.3 Å, respectively, Table 1) which indicate a limited interstratification. For this RH range, the minor mixed-layer structure contribution accounts for the high-angle asymmetry of 001 and 004 reflections and for the low-angle asymmetry of 003 and 005 ones.

At 0% RH, hydration of the Mg-SWy-1 is more heterogeneous with the presence of two mixed-layer structure contributions, one containing the three layer types and the other only 0W and 1W layers. The diffraction features of these two mixed-layer structures are quite similar, and the positional shift resulting from their contrasting compositions allows fitting the broad and diffuse maxima of the experimental XRD patterns.

DISCUSSION

Hydration properties of SWy-1 as a function of interlayer cation (Ca, Na, K)

The above quantitative description of the smectite hydration evolution is consistent with previous studies of smectite hydration (Sato et al. 1992, e.g.). The XRD pattern at 0% RH for sample K-SWy-1 exhibits a rational series of basal reflections because the structure is dominated by 0W layers (Figs. 3, 7a). A similar dehydrated state was described at 20% RH by Sato et al. (1992), although in the present study the evolution toward a more hydrated state occurs at this RH. However, the irrationally limit used by Sato et al. (1992) is not clearly defined, and the observed differences may result from a different threshold. The marked hydration heterogeneity observed by these authors over the 20-60% RH range is in agreement with the present study, but they reported a homogeneous mono-hydrated state at 80% RH in contrast to the significant proportion of 0W layers reported in the present work.

The description of Na-SWy-1 (Sato et al. 1992) is also consistent with the present data, with the only significant difference being the onset of the hydration process at low RH values (<20% RH) as observed here. In contrast, Sato et al. (1992) describe the transition between dehydrated and mono-hydrated states for RH values slightly higher than 20%. Finally, our study is consistent with that of Sato et al. (1992) for mostly homogeneous bi-hydrated state for Ca-SWy-1 over the 40-80% RH range, although they described the partial dehydration to the mono-hydrated state through highly heterogeneous structures for RH values of < 30%. At 0% RH, the *d*(001) value reported by Sato et al. (1992) is similar to our study, but they report a homogeneous hydration state for this RH in contrast to our results. Again, this difference may result from a different definition of the irrationality threshold in

538 the two studies. Similar hydration behavior of homoionic SWy-1 has also been reported by
539 Cases et al. (1992, 1997) and Bérend et al. (1995).
540
541 **Qualitative indicators of smectite hydration heterogeneity**
542 The ξ parameter, which accounts for the departure from rationality of 00ℓ reflections,
543 is a good indicator of the hydration-state heterogeneity. When heterogeneity increases from
544 the coexistence of different layer types, this parameter increases significantly in magnitude
545 (Fig. 8). Figure 8 plots the relative proportion of the prevailing layer type, whatever its nature,
546 as a function of the ξ parameter. Note the low proportion of XRD patterns (~25%) that were
547 modeled with >90% of the total layers of one layer type. However, even for homogeneous
548 samples, there is still a need to account for hydration heterogeneity to obtain a quality fit as
549 illustrated in Figure 9 for Li- and Mg-SWy-1. In these two samples, the prevailing layer type
550 (1W, and 2W layers, respectively) account for 92 and 83% of the total layers. However, it is
551 still necessary to consider other mixed-layer structure.
552 There is an approximately equal proportion of patterns that involve 70% or less of the
553 total layers attributed to one prevailing layer type as for 90% or more. Thus heterogeneity is
554 the rule rather than homogeneity for smectite hydration state. From Figure 8, note that the
555 increasing heterogeneity is correlated with an increase of the ξ parameter, which is larger than
556 0.4 Å when the prevailing layer type accounts for ~70% or less of the total layers. This
557 parameter is a good indicator of heterogeneity in the hydration state of smectite. The FWHM
558 of the 001 reflection, which is larger than 1.1° when the ξ parameter is larger than 0.4 Å, can
559 also be used for this purpose (Fig. 4). However, the dependence of the FWHM on the CSDS
560 leads to important variations of the former parameter even for low values of the ξ parameter.
561 For example, over a limited 0.00-0.15 range of the ξ parameter, the FWHM of the 001
562 reflection scatters from 0.47-1.07°2θ (Table 1). Larger variation of the FWHM parameter can

be expected if different samples are used. The use of the irrationality indicator (ξ parameter) to characterize hydration heterogeneity is thus preferable as recommended by Bailey (1982). However, the FWHM of the 001 reflection can be used as an alternative indicator of hydration heterogeneity by taking into account the evolution of 00ℓ reflection FWHM as a function of the ℓ index. After correction by cos θ to take into account crystal-size broadening, the FWHM of 00ℓ reflections should be about constant if hydration is homogeneous. Conversely, if hydration heterogeneity is important the evolution of this parameter is irregular.

In addition, in specific cases, hydration heterogeneity can be deduced directly from specific features of the experimental XRD patterns, related to 00ℓ line broadening. When heterogeneity arises from the coexistence of 0W and 1W layers (e.g. K-SWy-1 for RH = 20-80% and Na-SWy-1 at RH = 20%) there is no well-defined maximum on experimental XRD patterns between the 001 reflection (10.2-12.0 Å) and the maximum at ~3.1-3.2 Å. If heterogeneity results from the coexistence of 1W and 2W layers (e.g. Ca-SWy-1 at 20% RH), the maximum at ~3.1 Å is most affected and becomes broad. Finally, for highly hydrated smectite samples, a small proportion of 1W layers may be easily detected from the broadening of the 002 reflection at ~7.6 Å (e.g., see Sr-SWy-1 at 40 and 60% RH in Fig. 5d).

Smectite structure as a function of the nature of the interlayer cation and of relative humidity

Assessment of the smectite structure model. For almost all smectite samples described here, we considered two distinct contributions to the XRD profiles. These two contributions is a simplified approach to describe the hydration heterogeneity of the sample under investigation, with different layer types not being distributed at random in the different crystallites. The excellent quality of the fits clearly suggests that the proposed model is realistic. However, the use of two mixed-layer structures to fit all features of the XRD

588 patterns does not imply the actual presence of two populations of particles in the sample.
589 Accordingly, the relative proportions of the different mixed-layer structures contributing to
590 the diffracted intensity vary as a function of RH (Fig. 6). As a consequence, layers exhibiting
591 the same hydration state that are present in the different mixed-layer structures have identical
592 properties (Table 2) as they may be accounted for in one structure or the other depending on
593 the RH.

594 **Influence of the affinity of the interlayer cation for water.** For a given RH, the
595 relative proportion of the different layer types as a function of the cation ionic potential
596 (valency over ionic radius ratio, Fig. 10) may be given. Ionic radii considered here are given
597 by Shannon (1976) for octahedrally coordinated cations (1.38, 1.02, 0.76, 1.18, 1.00, and
598 0.72 Å for K^+, Na^+, Li^+, Sr^{2+}, Ca^{2+}, and Mg^{2+}, respectively). At 0% RH, 0W layers prevail in
599 K-, Na- and Sr-SWy-1, whereas Li-, Ca-, and Mg-SWy-1 are dominated by 1W layers. In Ca-
600 and Mg-SWy-1, some 2W layers are present despite the dry atmosphere. When increasing RH
601 to 20%, only K-SWy-1 remains mostly dehydrated, in agreement with its low affinity for H_2O
602 among the studied cations, whereas Na-, Li-, and Sr-SWy-1 are dominated by 1W layers.
603 Even at RH = 20%, Mg-SWy-1 is mostly bi-hydrated, in agreement with its high affinity for
604 H_2O, whereas Ca-SWy-1 exhibits an intermediate hydration state between 1W and 2W. At
605 35% RH, the only significant difference is the hydration state of Ca-SWy-1 which is
606 essentially bi-hydrated, whereas Sr-SWy-1 becomes so at 40% RH.. Finally, at 80% RH, all
607 samples are primarily bi-hydrated except K-SWy-1, which is dominated by 0W and 1W
608 layers in agreement with the low affinity of K^+ for H_2O. From the above results, the cation
609 ionic potential, which is directly related to the affinity of the cation for H_2O, allows a direct
610 comparison of the results obtained for all cations.

611 **Evolution of layer thickness with relative humidity.** Except for the omnipresence
612 of hydration heterogeneity, the modeling of experimental XRD patterns collected for a given

613 interlayer cation requires the consideration of variable layer-to-layer distance (i.e., layer
614 thickness) over the 0-80% RH range for a given layer type (1W, and 2W layers, Table 2). The
615 layer thickness is greater with increasing RH for all samples, whatever the interlayer cation
616 (Table 2). For samples displaying a stable and homogeneous hydration state over a large RH
617 interval (e.g., Li- and Mg-SWy-1) such an increase in layer thickness allowed to describe the
618 XRD patterns with a consistent structure model. In particular, it was possible to reproduce the
619 steady evolution of peak position without considering major interstratification effects. For 1W
620 layers, the increase of layer thickness is associated with an increased number of interlayer
621 H_2O molecules, except for K-SWy-1 at medium-to-high RH values. This apparent
622 inconsistency likely arises from the enhanced sensitivity of XRD to the basal spacing of the
623 different layer types as compared to their structure factors. As a consequence, layer thickness
624 has been systematically adjusted during the fitting process, whereas the amount of interlayer
625 H_2O was modified only when significant misfits were observed. A similar increase of
626 interlayer H_2O molecules and layer thickness is observed for 2W layers. However, for
627 monovalent cations the precision of the structural parameters determined for 2W layers is low
628 because of their low abundance (except at 80% RH for Na^+ and Li^+).

629 The interlayer thickness (IT), that is the layer thickness minus the thickness of the
630 2:1 layer (6.54 Å), is divided by the cation ionic radius and plotted as a function of RH (Fig.
631 11a). For each cation, a linear correlation was obtained between the weighted IT and the RH
632 value, which is expressed as:

633 $$\frac{IT}{r} = a \times RH + b \qquad \text{Equation 2}$$

634 where RH is expressed in % RH, r is the cation ionic radius expressed in Å, a and b represent
635 the slope and axial intercept, respectively. The regression lines obtained for the different
636 cations (Fig. 11a) show that their slopes increase with increasing cation ionic potential as
637 indicated, for example, by the comparison between Mg-SWy-1 and Na-SWy-1. For both 1W

and 2W layers, monovalent and divalent cations where compared by plotting these slopes as a function of the ionic potential (Fig. 11b), and successfully fitting a second order polynomial function to this data with ($r^2 \sim 0.99$):

$$a_{1W} = 3.525.10^{-1} \times \frac{v^2}{r^2} - 0.851.10^{-1} \times \frac{v}{r} \quad \text{Equation 3}$$

$$a_{2W} = 6.472.10^{-1} \times \frac{v^2}{r^2} - 5.433.10^{-1} \times \frac{v}{r} \quad \text{Equation 4}$$

where v is the cation valency. IT values weighted for the cation ionic radius obtained at 0% RH from the linear regression relationships shown in Figure 11a also correlates with the ionic potential for both 1W and 2W layer types ($r^2 = 0.95$ for the two linear regressions, Fig. 11c) leading to the following relations:

$$b_{1W} = -0.345 \times \frac{v}{r^2} + 6.099 \times \frac{1}{r} \quad \text{Equation 5}$$

$$b_{2W} = -0.914 \times \frac{v}{r^2} + 9.819 \times \frac{1}{r} \quad \text{Equation 6}$$

From the combination of the above two regression relations, it was thus possible to derive equations relating layer thickness to the RH value and to the ionic potential of cations:

$$\text{Layer thickness (1W)} = 12.639 - 0.345 \times \frac{v}{r} - 0.851.10^{-1} \times v \times RH + 3.525.10^{-1} \times \frac{v^2\,RH}{r} \quad \text{Equation 7}$$

$$\text{Layer thickness (2W)} = 16.359 - 0.914 \times \frac{v}{r} - 5.433.10^{-1} \times v \times RH + 6.472.10^{-1} \times \frac{v^2\,RH}{r} \quad \text{Equation 8}$$

which can be transformed to:

$$\text{Layer thickness (1W)} = 12.556 + 0.3525 \times \left(\frac{v}{r} - 0.241\right) \times (v \times RH - 0.979) \quad \text{Equation 9}$$

$$\text{Layer thickness (2W)} = 15.592 + 0.6472 \times \left(\frac{v}{r} - 0.839\right) \times (v \times RH - 1.412) \quad \text{Equation 10}$$

These equations allow the quantification of the steady increase of layer thickness with increasing RH for both 1W and 2W layers. Because the ionic potential of all cations considered here is higher than 0.241, the 1W layer-thickness value will increase systematically with increasing RH for all cations. For monovalent cations, 12.556 Å represents a maximum layer-thickness value for 1W layers whereas larger layer-thickness values may be obtained for divalent cations over the 50-100% RH range. Similarly, the 2W layer-thickness value will increase with increasing RH for all cations except K^+, whose ionic potential is lower than 0.839 Å. For K-saturated smectite, layer thickness should be about constant over the whole range of RH.

These results are consistent with those reported by Tamura et al. (2000) for synthetic smectite with a homogeneous layer-charge distribution, as they demonstrated that the hydration steps characterizing discrete hydration states (0W, 1W, 2W, … layers) do not correspond to fixed d-values. However, the present study demonstrates, in contrast to these authors, that the layer thickness increase also depends on the interlayer cation and on its ionic potential. From the above equations, it is possible to determine *a priori* the layer thickness for 1W and 2W low-charge montmorillonites for any interlayer cation. The validity of these equations for smectite with different amounts and location of charge needs to be assessed. Figures 11 and 12 show that the above regression equations lead to a realistic estimate of the experimentally determined layer thickness values for all samples except for 1W layers with interlayer Ca.

Interlayer H_2O. As described above, the increase of layer thickness as a function of RH is associated with an increase of the number of interlayer H_2O molecules (Table 2). Although this change was not systematic when comparing from one RH value to another, this increase was required to describe all XRD patterns. Together with an increase in the proportion of layers with higher hydration states, the greater number of interlayer H_2O with

681 increasing RH is essential for the increase in sample hydration. Interlayer H_2O is best
682 quantified using water vapor adsorption-desorption isotherms experiments (Cases et al. 1992,
683 1997; Bérend et al. 1995). With increasing RH, the combination of the average hydration state
684 of smectite and of the variable amount of interlayer H_2O molecules determined for each layer
685 type allows a reasonable estimate of the number of H_2O molecules in SWy-1 (Fig. 13). The
686 experimental water vapor adsorption-desorption data are not fitted as closely when a fixed
687 amount of interlayer H_2O molecules is considered, as usually assumed in the calculation of
688 XRD patterns involving hydrated smectites (Moore and Reynolds 1997, Fig. 13).

689 According to Moore and Reynolds (1997), interlayer cations are sandwiched between
690 partial planes of H_2O molecules [0.69 H_2O per $O_{20}(OH)_4$] located at 0.35 and 1.06 Å from the
691 cation along the c^* axis. A third and denser plane [1.20 H_2O per $O_{20}(OH)_4$] is located further
692 from the central interlayer cation at 1.20 Å along the c^* axis. In our study, XRD patterns were
693 modeled for 2W layers by defining a unique plane of H_2O molecules on each side of the
694 central interlayer cation. This plane is located at 1.20 Å from the central interlayer cation
695 along the c^* axis. This plane is analogous to the dense plane of H_2O molecules of Moore and
696 Reynolds (1997). By using the hydration heterogeneity determined above for Sr-Swy-1 at
697 80% RH, it is possible to fit satisfactorily the 001 reflection using the positions of interlayer
698 species proposed by Moore and Reynolds (1997, Fig. 14). However, the interlayer positions
699 and the associated interlayer species proposed by Moore and Reynolds (1997) produced an
700 intensity distribution dramatically different from the experimental data for higher-angle
701 reflections (Fig. 14). No attempt was made here to further refine the z-coordinate of the H_2O
702 plane as a function of interlayer cation ionic radius.

703 **Fluctuation in atomic z-coordinates - σ_z parameter.** Two trends are obtained for
704 the σ_z parameter (Table 2), which corresponds to fluctuation of layer thickness, obtained for
705 the different samples. First, high values for σ_z are often observed for highly heterogeneous

706 samples (e.g., Li-SWy-1 at 0% RH, Ca-SWy-1 at 0 and 20% RH). These high values may
707 result from the incomplete transition of a given interlayer from one hydration state to the next.
708 As a result different hydration states would coexist within a given interlayer leading to a large
709 variation of the interlayer thickness.

710 Second, the σ_z parameter is usually significantly higher (0.25-0.52 Å) when the
711 sample is saturated with divalent cations rather than monovalent cations (0.15-0.25 Å, except
712 for the Li-SWy-1 sample at 0% RH). This behavior may be related to two possible structural
713 features. The first feature relates to the valencies of the cations. The density of divalent
714 cations is half that of monovalent cations, which produces an extremely heterogeneous
715 distribution of electrostatic interactions between the 2:1 layer and interlayer cations. This
716 heterogeneous distribution could perhaps induce fluctuations of the layer thickness within a
717 given interlayer allowed by the flexibility of the 2:1 layers. The second structural feature for
718 such an increased σ_z parameter probably relates to the affinity of divalent cations for the bi-
719 hydrated state. The higher layer thickness observed for 2W layers implies weaker electrostatic
720 interactions between the negatively charged layer and the interlayer cations. Consequently,
721 the position of interlayer cations with respect to the 2:1 layer is weakly constrained and the
722 resulting variation of layer thickness from one interlayer to an adjacent interlayer is greater.
723 However, the affinity of divalent cations for 2W layers is probably a second-order influence
724 as shown by the low values for the σ_z parameter on Na- and Li-SWy-1 at 80% RH, even
725 though these two samples are dominated by 2W layers.

726 **Size of the CSD (N) and sample orientation (σ*).** The CSD size along the *c** axis
727 determined for each sample is globally stable over the entire RH range investigated (Table 2).
728 However, a small decrease of the CSD size is systematically observed at RH = 0% for
729 monovalent interlayer cations. Except for the Li-SWy-1 sample, these samples are strongly
730 dehydrated with a high proportion (>95%) of 0W layers. Such dehydration probably increases

731 porosity, including intra-crystalline porosity, that could reduce the CSD size. This observation
732 is supported by the non-variance of the N value at low RH for smectite having divalent
733 interlayer cations (Table 2). Consistently, σ* values determined for these dehydrated samples
734 were systematically higher than those adjusted for higher RH values, possibly as a result of
735 the textural modifications resulting from increased porosity. However, the increase of σ* is
736 observed even for SWy-1 samples exchanged with divalent cations, possibly as an early
737 indication of the ongoing dehydration process.

738 Lower values of N were also determined for each sample at high RH values (60-
739 80%) possibly as the result of the splitting of some layer stacks induced by the "osmotic"
740 swelling of some smectite interlayers. No significant change of the sample orientation is
741 observed at these high RH values pleading for a different origin for the N decrease, as
742 compared to the low RH conditions. In our study, lower N values may thus possibly indicate
743 the presence of a small number of 3W layers that are not accounted for in the calculation, but
744 such layers would disrupt the stacking order. This hypothesis is consistent with the transition
745 from 2W to 3W smectite which occurs for RH values higher than 90% for Ca-exchanged
746 smectites (Watanabe and Sato 1988).

747 **Possible improvements to the proposed description.** The fluctuations of N and σ*
748 described above may also result from the difficulty in fitting the low-angle region of
749 experimental XRD patterns. The calculated patterns are always intense over this angular range
750 as compared to experimental ones. The alternative model proposed by Plançon (2002) for the
751 description of layer stacking in crystals could possibly better account for such textural defects
752 in the stacking sequences. In this model, particles rather than crystals are considered. Particles
753 have sizes larger than crystals and contain defects such as cracks, inner-porosity, bent layers,
754 edge dislocations, etc. These defects disrupt the periodic layer stacking by inducing variations
755 in the *d*-value that are accounted for in the proposed formalism. XRD patterns calculated

using this formalism nearly coincide with those calculated in our study except in the low-angle region (<5°2θ Cu Kα, Plançon 2002), and thus do not challenge the structure models described in the present work. Over the low-angle region, XRD patterns calculated using the formalism of Plançon (2002) exhibit a much lower background intensity which would fit better the experimental XRD data. According to this alternative model, the observed decrease of N is described as the increased frequency of defects whereas the overall size of the "particles" would probably be constant.

In addition, our study shows that the positions and concentrations of interlayer species proposed by Moore and Reynolds (1997) are incorrect. Although the quality of the models obtained in our study is satisfactory, structural parameters may possibly be further refined by utilizing hydration heterogeneity.

ACKNOWLEDGMENTS

The results presented are a part of a Ph.D. thesis granted by Andra (French National Agency for Nuclear Waste Disposal). Andra is thanked for the permission to publish this manuscript and for financial support. BL acknowledges financial support from the CNRS/PICS709 program, and from the CNRS/SdU "postes rouges" fellowships granted to BAS. VAD and BAS are grateful to the Russian Science Foundation for partial financial support. Laurent Michot (LEM, Nancy – France) is thanked for the fruitful discussions about smectite hydration. The manuscript was much improved by the constructive reviews of Javier Cuadros, Dougal Mc Carty, and AE Steve Guggenheim, and by the remarks of Emmanuel Jacquot on an early version of the manuscript. The editorial assistance of AE Steve Guggenheim is acknowledged.

REFERENCES CITED

Bailey, S.W. (1982) Nomenclature for regular interstratifications. American Mineralogist, 67, 394-398.

Bauer, A. and Berger, G. (1998) Kaolinite and smectite dissolution rate in high molar KOH solutions at 35°C and 80°C. Applied Geochemistry, 13, 905-916.

Bauer, A. and Velde, B. (1999) Smectite transformation in high molar KOH solutions. Clay Minerals, 34, 259-273.

Bauer, A., Velde, B., and Berger, G. (1998) Kaolinite transformation in high molar KOH solutions. Applied Geochemistry, 13, 619-629.

Beaufort, D., Berger, G., Lacharpagne, J.C., and Meunier, A. (2001) An experimental alteration of montmorillonite to a di + trioctahedral smectite assemblage at 100 and 200°C. Clay Minerals, 36, 211-225.

Ben Brahim, J., Armagan, N., Besson, G., and Tchoubar, C. (1983a) X-ray diffraction studies on the arrangement of water molecules in a smectite. I. Two-water-layer Na-beidellite. Journal of Applied Crystallography, 16, 264-269.

Ben Brahim, J., Besson, G., and Tchoubar, C. (1983b) Layer succession and water molecules arrangement in a homogeneous two-water layer Na-smectite. 5th Meeting of the European Clay Groups, p. 65-75, Prague.

-------- (1984) Etude des profils des bandes de diffraction X d'une beidellite-Na hydratée à deux couches d'eau. Détermination du mode d'empilement des feuillets et des sites occupés par l'eau. Journal of Applied Crystallography, 17, 179-188.

Bérend, I., Cases, J.M., François, M., Uriot, J.P., Michot, L.J., Masion, A., and Thomas, F. (1995) Mechanism of adsorption and desorption of water vapour by homoionic

montmorillonites: 2. The Li^+, Na^+, K^+, Rb^+ and Cs^+ exchanged forms. Clays & Clay Minerals, 43, 324-336.

Bradley, W.F., Grim, R.E., and Clark, G.F. (1937) A study of the behavior of montmorillonite on wetting. Zeitschrift Kristallographie, 97, 260-270.

Burst, J.F. (1969) Diagenesis of Gulf Coast clayey sediments and its possible relation to petroleum migration. American Association of Petroleum Geologists Bulletin, 53, 73-93.

Calarge, L., Lanson, B., Meunier, A., and Formoso, M.L. (2003) The smectitic minerals in a bentonite deposit from Melo (Uruguay). Clay Minerals, 38, 25-34.

Cama, J., Ganor, J., Ayora, C., and Lasaga, C.A. (2000) Smectite dissolution kinetics at 80 degrees C and pH 8.8. Geochimica & Cosmochimica Acta, 64, 2701-2717.

Carroll, S.A. and Walther, J.V. (1990) Kaolinite dissolution at 25°, 60° and 80°C. American Journal of Science, 290, 797-810.

Carroll-Webb, S.A. and Walther, J.V. (1988) A surface complex reaction model for the pH-dependence of corundum and kaolinite dissolution. Geochimica & Cosmochimica Acta, 2609-2623.

Cases, J.M., Bérend, I., Besson, G., François, M., Uriot, J.P., Thomas, F., and Poirier, J.P. (1992) Mechanism of adsorption-desorption of water vapor by homoionic montmorillonite. 1. The sodium exchanged form. Langmuir, 8, 2730-2739.

Cases, J.M., Bérend, I., François, M., Uriot, J.P., Michot, L.J., and Thomas, F. (1997) Mechanism of adsorption and desorption of water vapour by homoionic montmorillonite: 3. The Mg^{2+}, Ca^{2+}, Sr^{2+} and Ba^{2+} exchanged forms. Clays & Clay Minerals, 45, 8-22.

828 Chermak, J.A. (1992) Low temperature experimental investigation of the effect of high pH
829 NaOH solutions on the opalinus shale, switzerland. Clays & Clay Minerals, 40, 650-
830 658.
831 -------- (1993) Low temperature experimental investigation of the effect of high pH KOH
832 solutions on the Opalinus shale, Switzerland. Clays & Clay Minerals, 41, 365-372.
833 Claret, F., Bauer, A., Schafer, T., Griffault, L., and Lanson, B. (2002) Experimental
834 Investigation of the interaction of clays with high-pH solutions: a case study from the
835 Callovo-Oxfordian formation, Meuse-Haute Marne underground laboratory (France).
836 Clays & Clay Minerals, 50, 633-646.
837 Cuadros, J. (1997) Interlayer cation effects on the hydration state of smectite. American
838 Journal of Science, 297, 829-841.
839 Drits, V.A., Lindgreen, H., Sakharov, B.A., and Salyn, A.S. (1997a) Sequential structure
840 transformation of illite-smectite-vermiculite during diagenesis of Upper Jurassic shales,
841 North Sea. Clay Minerals, 33, 351-371.
842 Drits, V.A. and Sakharov, B.A. (1976) X-Ray structure analysis of mixed-layer minerals. 256
843 p. Dokl. Akad. Nauk SSSR, Moscow.
844 Drits, V.A., Sakharov, B.A., Salyn, A.L., and Lindgreen, H. (2005) Determination of the
845 content and distribution of fixed ammonium in illite-smectite using a modified X-ray
846 diffraction technique: Application to oil source rocks of western Greenland. American
847 Mineralogist, 90, in press.
848 Drits, V.A., Srodon, J., and Eberl, D.D. (1997b) XRD measurement of mean crystallite
849 thickness of illite and illite/smectite: reappraisal of the kubler index and the scherrer
850 equation. Clays & Clay Minerals, 45, 461-475.

851 Drits, V.A. and Tchoubar, C. (1990) X-ray diffraction by disordered lamellar structures:
852 Theory and applications to microdivided silicates and carbons. 371 p. Springer-Verlag,
853 Berlin.
854 Drits, V.A., Varaxina, T.V., Sakharov, B.A., and Plançon, A. (1994) A simple technique for
855 identification of one-dimensional powder X-Ray diffraction patterns for mixed-layer
856 illite-smectites and other interstratified minerals. Clays & Clay Minerals, 42, 382-390.
857 Eberl, D.D., Velde, B., and Mc Cormick, T. (1993) Synthesis of illite-smectite from smectite
858 at Earth surface temperatures and high pH. Clay Minerals, 28, 49-60.
859 Glaeser, P.R. and Méring, J. (1954) Isothermes d'hydratation des montmorillonites bi-
860 ioniques (Ca, Na). Clay Mineral Bulletin, 2, 188-193.
861 Glaeser, R., Mantine, I. and Méring, J. (1967) Observations sur la beidellite. Bulletin du
862 Groupe Français des Argiles, 19, 125-130.
863 Glaeser, R. and Méring, J. (1968) Domaines d'hydratation des smectites. Comptes-Rendus de
864 l'Académie des Sciences de Paris, 267, 463-466.
865 Guinier, A. (1964) Théorie et technique de la radiocristallographie. 740 p. Dunod, Paris.
866 Harward, M.E. and Brindley, G.W. (1965) Swelling properties of synthetic smectites in
867 relation to lattice substitutions. Clays & Clay Minerals, 13, 209-222.
868 Harward, M.E., Carstea, D.D., and Sayegh, A.H. (1969) Properties of vermiculites and
869 smectites: expansion and collapse. Clays & Clay Minerals, 16, 437-447.
870 Howard, S.A. and Preston, K.D. (1989) Profile fitting of powder diffraction patterns. In D.L.
871 Bish, and J.E. Post, Eds. Modern Powder Diffraction, 20, p. 217-275. Mineralogical
872 Society of America, Wahington D.C.
873 Hower, J., Eslinger, E.V., Hower, M.E., and Perry, E.A. (1976) Mechanism of burial
874 metamorphism of argillaceous sediments: 1. Mineralogical and chemical evidence.
875 Geological Society of America Bulletin, 87, 725-737.

876 Hower, J. and Mowatt, T.C. (1966) The mineralogy of illites and mixed-layer
877 illite/montmorillonites. American Mineralogist, 51, 825-854.
878 Huang, W.L. (1993) The formation of illitic clays from kaolinite in KOH solution from 225°C
879 to 350°C. Clays & Clay Minerals, 41, 645-654.
880 Huertas, F.J., Caballero, E., de Cisneros, C.J., Huertas, F., and Linares, J. (2001) Kinetics of
881 montmorillonite dissolution in granitic solutions. Applied Geochemistry, 16, 397-407.
882 Iwasaki, T. and Watanabe, T. (1988) Distribution of Ca and Na ions in dioctahedral smectites
883 and interstratified dioctahedral mica/smectites. Clays & Clay Minerals, 36, 73-82.
884 Kittrick, J.A. (1969a) Interlayer forces in montmorillonite and vermiculite. Soil Science
885 Society of America Journal, 33, 217-222.
886 -------- (1969b) Quantitative evaluation of the strong-force model for expansion and
887 contraction of vermiculite. Soil Science Society of America Journal, 33, 222-225.
888 Laird, D.A. (1996) Model for crystalline swelling of 2:1 phyllosilicates. Clays & Clay
889 Minerals, 44, 553-559.
890 -------- (1999) Layer charge influences on the hydration of expandable 2:1 phyllosilicates.
891 Clays & Clay Minerals, 47, 630-636.
892 Levy, R. and Francis, C.W. (1975) Demixing of sodium and calcium ions in montmorillonite
893 crystallites. Clays & Clay Minerals, 23, 475-476.
894 Mamy, J. and Gaultier, J.P. (1979) Etude comparée de l'évolution des montmorillonites
895 biioniques K-Ca de Camp-Berteaux et du Wyoming sous l'effet des cycles
896 d'humectation et de déssication. Clay Minerals, 14, 181-192.
897 Méring, J. (1949) L'interférence des rayons-X dans les systèmes à stratification désordonnée.
898 Acta Crystallographica, 2, 371-377.

899 Méring, J. and Glaeser, P.R. (1954) Sur le rôle de la valence des cations échangeables dans la
900 montmorillonite. Bulletin de la Société Francaise de Minéralogie et Cristallographie, 77,
901 519-530.
902 Mermut, A.R. and Lagaly, G. (2001) Baseline studies of The Clay Mineral Society Source
903 Clays: layer-charge determination and characteristics of those minerals containing 2:1
904 layers. Clays & Clay Minerals, 49, 393-397.
905 Meunier, A., Lanson, B., and Velde, B. (2004) Composition variation of illite-vermiculite-
906 smectite mixed-layer minerals in a bentonite bed from Charente (France). Clay
907 Minerals, 39, 317-332.
908 Mohnot, S.M., Bae, J.H., and Foley, W.L. (1987) A study of alkali/mineral reactions. SPE
909 Reservoir Engineering, Nov. 1987, 653-663.
910 Mooney, R.W., Keenan, A.G., and Wood, L.A. (1952) Adsorption of water by
911 montmorillonite. II. Effect of exchangeable ions and lattice swelling as measured by X-
912 ray diffraction. Journal of American Chemical Society, 74, 1371-1374.
913 Moore, D.M. and Hower, J. (1986) Ordered interstratification of dehydrated and hydrated Na-
914 smectite. Clays & Clay Minerals, 34, 379-384.
915 Moore, D.M. and Reynolds, R.C., Jr (1997) X-ray Diffraction and the Identification and
916 Analysis of Clay Minerals. 322 p. Oxford University Press, Oxford and New York.
917 Nagelschmidt, G. (1936) The structure of montmorillonite. Zeitschrift Kristallographie, 93,
918 481-487.
919 Norrish, K. (1954) The swelling of montmorillonite. Discussions of the Faraday society, 18,
920 120-133.
921 Perry, E.A., Jr and Hower, J. (1972) Late-stage dehydration in deeply buried pelitic
922 sediments. American Association of Petroleum Geologists Bulletin, 56, 2013-2021.

923 Plançon, A. (2002) New modeling of X-ray diffraction by disordered lamellar structures, such
924 as phyllosilicates. American Mineralogist, 87, 1672-1677.
925 Rassineux, F., Griffault, L., Meunier, A., Berger, G., Petit, S., Viellard, P., Zellagui, R., and
926 Munoz, M. (2001) Expandability-layer stacking relationship during experimental
927 alteration of a Wyoming bentonite in pH 13.5 solutions at 35 and 60°C. Clay Minerals,
928 36, 197-210.
929 Sakharov, B.A., Lindgreen, H., Salyn, A., and Drits, V.A. (1999) Determination of illite-
930 smectite structures using multispecimen X-Ray diffraction profile fitting. Clays & Clay
931 Minerals, 47, 555-566.
932 Sato, T., Murakami, T., and Watanabe, T. (1996) Change in layer charge of smectites and
933 smectite layers in illite/smectite during diagenetic alteration. Clays & Clay Minerals, 44,
934 460-469.
935 Sato, T., Watanabe, T., and Otsuka, R. (1992) Effects of layer charge, charge location, and
936 energy change on expansion properties of dioctahedral smectites. Clays & Clay
937 Minerals, 40, 103-113.
938 Shannon, R.D. (1976) Revised effective ionic radii and systematic studies of interatomic
939 distances in halides and chalcogenides. Acta Crystallographica, A 32, 751-767.
940 Stucki, J.W., Golden, D.C., and Roth, C.B. (1984) Effects of reduction and reoxidation of
941 structural iron on the surface charge dissolution of dioctahedral smectites. Clays & Clay
942 Minerals, 32, 350-356.
943 Tamura, K., Yamada, H., and Nakazawa, H. (2000) Stepwise hydration of high-quality
944 synthetic smectite with various cations. Clays & Clay Minerals, 48, 400-404.
945 Taubald, H., Bauer, A., Schafer, T., Geckeis, H., Satir, M., and Kim, J.I. (2000) Experimental
946 investigation of the effect of high-pH solutions on the Opalinus Shale and the
947 Hammerschmiede Smectite. Clay Minerals, 35, 515-524.

948 Van Olphen, H. (1965) Thermodynamics of interlayer adsorption of water in clays. Journal of
949 Colloid Science, 20, 822-837.
950 Walker, G.F. (1956) The mechanism of dehydration of Mg-vermiculite. Clays & Clay
951 Minerals, 4, 101-115.
952 Watanabe, T. and Sato, T. (1988) Expansion characteristics of montmorillonite and saponite
953 under various relative humidity conditions. Clay Science, 7, 129-138.
954 Weaver, C.E. (1960) Possible uses of clay minerals in search for oil. American Association of
955 Petroleum Geologists Bulletin, 44, 1505-1518.
956 Yamada, H., Nakazawa, H., Hashizume, H., Shimomura, S., and Watanabe, T. (1994)
957 Hydration behavior of Na-smectite crystals synthetised at high pressure and high
958 temperature. Clays & Clay Minerals, 42, 77-80.
959

FIGURE CAPTIONS

FIGURE 1. Influence on calculated XRD patterns of the cumulative deviation of the layer thickness from the strict *d*(001) periodicity. This deviation is quantified here study with the σ_z parameter. The effect is shown for a XRD pattern calculated for a pure bi-hydrated Ca-SWy-1 sample. Solid line: σ_z = 0.0 Å, gray line: σ_z = 0.3 Å.

FIGURE 2. Basic principle of the strategy used to fit experimental XRD patterns (see text for details). **a**) The experimental pattern of sample K-SWy-1 recorded at 0% RH is shown as crosses, whereas the XRD pattern calculated for a pure dehydrated smectite (100% 0W layers) is shown as a gray line. Values in parentheses correspond to ℓ×d(00ℓ) ideal positions. **b**) The maxima of the difference plot between experimental and calculated patterns are located between elementary contributions corresponding to 0W and 1W layer types (light and dark gray ticks, respectively). **c**) The optimum fit to the experimental data, shown as a solid line, consists of a mixture of the initial pure dehydrated structure with a mixed-layer structure (70:30 ratio between 1W and 0W layers). These two elementary contributions are shown as bold gray and solid lines, respectively. **d**) Schematic representation of the structure model used to fit the experimental XRD pattern. Relative proportions, expressed in wt%, of the two elementary mixed-layer structure contributions are plotted on the y-axis whereas their compositions (relative proportions of the different layer types) are plotted on the x-axis. Light gray and dark gray bars represent 0W and 1W layers, respectively.

FIGURE 3. Variations of the basal spacing *d*(001) measured on experimental XRD patterns as a function of relative humidity for samples saturated with monovalent and divalent cations. *d*(001) values are plotted as open symbols when the departure from rationality parameter (ξ) determined for the basal reflection series (see text for

details) is higher than 0.4 Å. Light gray areas represent commonly reported *d*(001) values reported for bi-hydrated (*d*(001) at 15.0-15.8 Å), mono-hydrated (*d*(001) at 12.3-12.7 Å) and dehydrated smectites (*d*(001) at 9.6-10.1 Å).

FIGURE 4. FWHM of the (001) reflection as a function of the departure from rationality parameter ξ (see text for details). Values of these two parameters (1.1°2θ Cu Kα, and 0.4 Å, respectively) limiting the "homogeneous" hydration domains are shown as dotted lines. Open and solid symbols as in Figure 3.

FIGURE 5. Comparison between experimental and calculated XRD patterns as a function of RH. Experimental and calculated optimal XRD patterns are shown as crosses and as solid lines, respectively. Difference plots are shown at the bottom of the figure. **a**) Sample K-SWy-1. **b**) Sample Na-SWy-1. **c**) Sample Li-SWy-1. **d**) Sample Sr-SWy-1. **e**) Sample Ca-SWy-1. **f**) Sample Mg-SWy-1. For Na-, Li-, Sr-, Ca- and Mg-SWy-1 samples, the gray bar indicates a modified scale factor for the high-angle region. Dashed lines in Figure 5f indicate the ideal peak positions for 2W smectite (15.8 Å).

FIGURE 6: Structure models obtained from XRD profiles modeling for all samples as a function of RH. Symbols and notations as in Figure 2d (solid bars represent 2W layers).

FIGURE 7. Evolution of the relative abundance of different layer types (including all mixed-layer structures) as a function of RH for all samples. **a**) Sample K-SWy-1. **b**) Sample Na-SWy-1. **c**) Sample Li-SWy-1. **d**) Sample Sr-SWy-1. **e**) Sample Ca-SWy-1. **f**) Sample Mg-SWy-1. Triangles, diamonds, and squares represent 0W, 1W and 2W layers, respectively.

FIGURE 8. Relative proportion of the major layer type (whatever its nature) derived from XRD profile modeling as a function of the departure from rationality parameter ξ. Dotted lines as in Figure 4; solid and open symbols as in Figure 3.

1009 **FIGURE 9.** Comparison between the experimental XRD patterns obtained for Li- and Mg-
1010 SWy-1 samples at 40% RH and that calculated considering only the most
1011 homogeneous phase from the optimum structure models reported in Figure 6.
1012 **FIGURE 10.** Relative proportion of the different layer types determined at each RH for the
1013 different samples. Samples are ranked as a function of their ionic potential (v/r).
1014 Light gray, dark gray and solid bars represent 0W, 1W, and 2W layers, respectively.
1015 **FIGURE 11.** Evolution of layer thickness as a function of RH for all samples. Evolutions for
1016 1W and 2W layer types are shown on the left and right columns, respectively. **a**)
1017 Evolution of the interlayer thickness (IT), that is layer thickness minus the thickness
1018 of the 2:1 layer (6.54Å), weighted for the cation ionic radius as a function of RH for
1019 all samples. Linear regression lines are plotted for each cation. **b**) Evolution of the
1020 slope of the linear regressions shown on Figure 11a as a function of the ionic
1021 potential of the interlayer cation. A 2^{nd} order polynomial regression is fitted to this
1022 data. **c**) Evolution of the IT weighted for the cation ionic radius at 0% RH obtained
1023 from the linear regression shown on Figure 11a as a function of the ionic potential of
1024 the interlayer cation. A linear regression is fitted to this data.
1025 **FIGURE 12.** Comparison between the layer-thickness values determined for 1W and 2W
1026 layers from Equations 7 and 8, respectively, with that obtained from XRD profile
1027 modeling. Linear regressions are fitted to the data. **a**) 1W layers. **b**) 2W layers.
1028 **FIGURE 13.** Comparison between the amount of water determined from water vapor
1029 adsorption-desorption isotherms by Bérend et al. (1995) and Cases et al. (1997) and
1030 that derived from XRD profile modeling. Adsorption and desorption pathways are
1031 shown as solid and dashed lines, respectively. Solid and open patterns indicate
1032 results derived from the modeling of XRD patterns recorded in adsorption and
1033 desorption conditions, respectively. Triangles indicate results derived from the

modeling of XRD patterns assuming the fixed amount of interlayer H_2O molecules commonly used in the calculation of XRD patterns involving hydrated smectites (Moore and Reynolds 1997). Squares indicate results derived from the modeling of XRD patterns assuming a variable amount of interlayer H_2O molecules as described here. Gray patterns indicate the starting conditions (~35% RH).

FIGURE 14. Comparison of the experimental XRD pattern recorded for Sr-SWy-1 sample at 80% RH with that calculated using a structure model similar to the optimal one (Table 2) but replacing the refined atomic positions for interlayer H_2O molecules by that proposed by Moore and Reynolds (1997). Patterns as in Figure 2a.

TABLES

TABLE 1. Evolution of the basal reflection qualitative describers (position, width and rationality) as a function of relative humidity.

Sample	K			Na			Li		
	d(001)	FWHM	ξ, X_i	*d*(001)	FWHM	ξ, X_i	*d*(001)	FWHM	ξ, X_i
~0%	10.24	1.07	0.14, 3	9.75	0.85	0.07, 4	11.66	1.39	0.52, 3
20%	10.95	1.53	0.64, 3	11.96	1.17	0.53, 4	12.31	0.59	0.04, 4
~35%	11.36	1.57	0.86, 3	12.44	0.68	0.10, 3	12.32	0.58	0.04, 4
40%	11.54	1.51	1.34, 2	12.45	0.66	0.02, 3	12.33	0.59	0.03, 4
60%	11.57	1.51	1.34, 2	12.47	0.72	0.01, 3	12.36	0.66	0.04, 4
80%	12.04	1.82	1.69, 2	15.28	0.75	0.28, 3	15.49	0.73	0.28, 4

Sample	Sr			Ca			Mg		
	d(001)	FWHM	ξ, X_i	*d*(001)	FWHM	ξ, X_i	*d*(001)	FWHM	ξ, X_i
~0%	10.34	0.82	0.28, 4	11.72	1.12	0.50, 4	11.50	1.25	0.45, 4
20%	12.40	0.54	0.02, 4	13.98	1.24	0.93, 4	14.00	0.97	0.28, 4
~35%	12.41	0.51	0.03, 4	14.97	0.70	0.27, 4	14.11	0.98	0.31, 4
40%	15.28	0.56	0.14, 4	15.02	0.72	0.27, 4	14.83	0.81	0.17, 4
60%	15.56	0.47	0.06, 4	15.25	0.67	0.23, 4	15.44	0.78	0.28, 4
80%	15.75	0.47	0.06, 4	15.43	0.68	0.20, 4	15.82	0.70	0.14, 4

Note: Position (*d*(001)) and FWHM of the 001 reflection are given in Å and in °2θ Cu Kα, respectively. The ξ parameter which accounts for the departure from rationality of the 00ℓ reflection series is calculated as the standard deviation of the ℓ×*d*(00ℓ) values calculated for the X_i measurable reflections over the 2-50°2θ Cu Kα angular range

TABLE 2. Optimum structural parameters used for the simulation of XRD profiles.

			K-SWy			
RH	0	20	room	40	60	80
L. Tck. 2W	-	15.55	15.55	15.55	15.55	15.55
nH_2O		2×3.2	2×3.2	2×3.2	2×3.2	2×3.2
L. Tck. 1W	12.40	12.42	12.50	12.55	12.60	12.65
nH_2O	2.0	4.0	4.0	4.0	4.0	4.0
L. Tck. 0W	10.00	10.00	10.00	10.00	10.00	10.00
N	7.5	12.0	11.0	12.0	13.0	9.0
σ^*	4.0	5.0	5.0	5.0	5.0	5.0
σ_z	0.25	0.20	0.20	0.20	0.20	0.20
			Na-SWy			
RH	0	20	room	40	60	80
L. Tck. 2W	-	15.40	15.45	15.45	15.45	15.45
nH_2O		2×3.2	2×3.2	2×3.2	2×3.5	2×3.5
L. Tck. 1W	12.30	12.37	12.45	12.46	12.47	12.55
nH_2O	2.8	3.0	3.3	3.6	3.8	4.5
L. Tck. 0W	9.60	9.60	9.60	9.60	9.60	9.8
N	7.5	9.5	7.5	7.5	7.0	6.5
σ^*	6.0	5.0	3.2	2.8	3.0	2.8
σ_z	0.15	0.15	0.22	0.25	0.22	0.17
			Li-SWy			
RH	0	20	room	40	60	80
L. Tck. 2W	-	15.50	15.55	15.55	15.55	15.75
nH_2O		2×2.6	2×2.6	2×2.6	2×2.6	2×3.2
L. Tck. 1W	12.10	12.255	12.265	12.28	12.296	12.40
nH_2O	2.2	3.7	3.9	3.9	4.2	4.2
L. Tck. 0W	9.60	9.60	9.60	9.60	9.60	9.60
N	7.0	9.5	9.5	9.0	7.8	7.5
σ^*	10.0	6.0	6.0	6.0	6.0	3.7
σ_z	0.40	0.23	0.23	0.23	0.23	0.20

Sr-Swy						
RH	0	20	room	40	60	80
L. Tck. 2W	-	15.10	15.30	15.30	15.53	15.73
nH_2O		2×2.5	2×3.0	2×3.0	2×3.0	2×3.0
L. Tck. 1W	11.90	12.35	12.35	12.40	12.58	12.70
nH_2O	2.0	3.0	3.0	3.5	3.5	5.5
L. Tck. 0W	9.80	10.00	10.00	10.00	10.00	10.00
N	11.0	10.0	10.0	9.0	7.5	7.5
σ^*	10.0	6.0	6.0	5.5	5.5	5.5
σ_z	0.25	0.25	0.25	0.30	0.35	0.35
Ca-SWy						
RH	0	20	room	40	60	80
L. Tck. 2W	14.30	14.79	15.10	15.11	15.30	15.51
nH_2O	2×2.5	2×2.6	2×3.3	2×3.3	2×3.3	2×3.3
L. Tck. 1W	11.65	12.58	12.75	12.76	12.80	12.85
nH_2O	1.5	3.2	3.2	3.2	3.2	3.2
L. Tck. 0W	10.00	10.00	10.00	10.00	10.00	10.00
N	8.0	8.0	8.0	8.0	7.0	6.0
σ^*	7	11.0	7.0	7.5	7.0	6.5
σ_z	0.35	0.36	0.27	0.27	0.27	0.27
Mg-Swy						
RH	0	20	room	40	60	80
L. Tck. 2W	13.90	14.20	14.45	14.80	15.42	15.80
nH_2O	2×1.73	2×1.73	2×1.73	2×3.0	2×3.0	2×3.2
L. Tck. 1W	11.50	12.10	12.30	12.50	12.70	13.00
nH_2O	2.5	2.5	3.0	3.0	3.5	3.5
L. Tck. 0W	10.00	10.00	10.00	10.00	10.00	10.00
N	8.0	8.0	7.0	6.5	6.5	6.0
σ^*	9.0	5.5	5.2	5.2	5.2	5.2
σ_z	0.45	0.45	0.45	0.52	0.52	0.52

Note: Layer thickness (L. Tck.) of bi-hydrated, mono-hydrated and dehydrated layers (2W, 1W and 0W layers, respectively) are given in Å. For hydrated layers, the amount of interlayer H_2O molecules is indicated per $O_{20}(OH)_4$. N is the mean number of layers in the coherent scattering domain, orientation parameter σ^* and layer thickness variability parameter (σ_z) are given in ° and in Å, respectively.

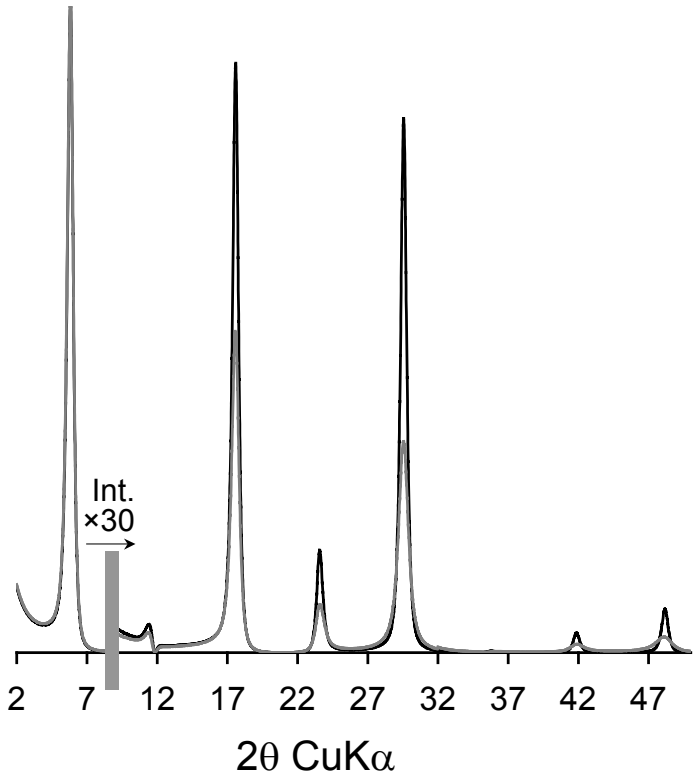

Ms#1776 Ferrage et al. Fig. 01

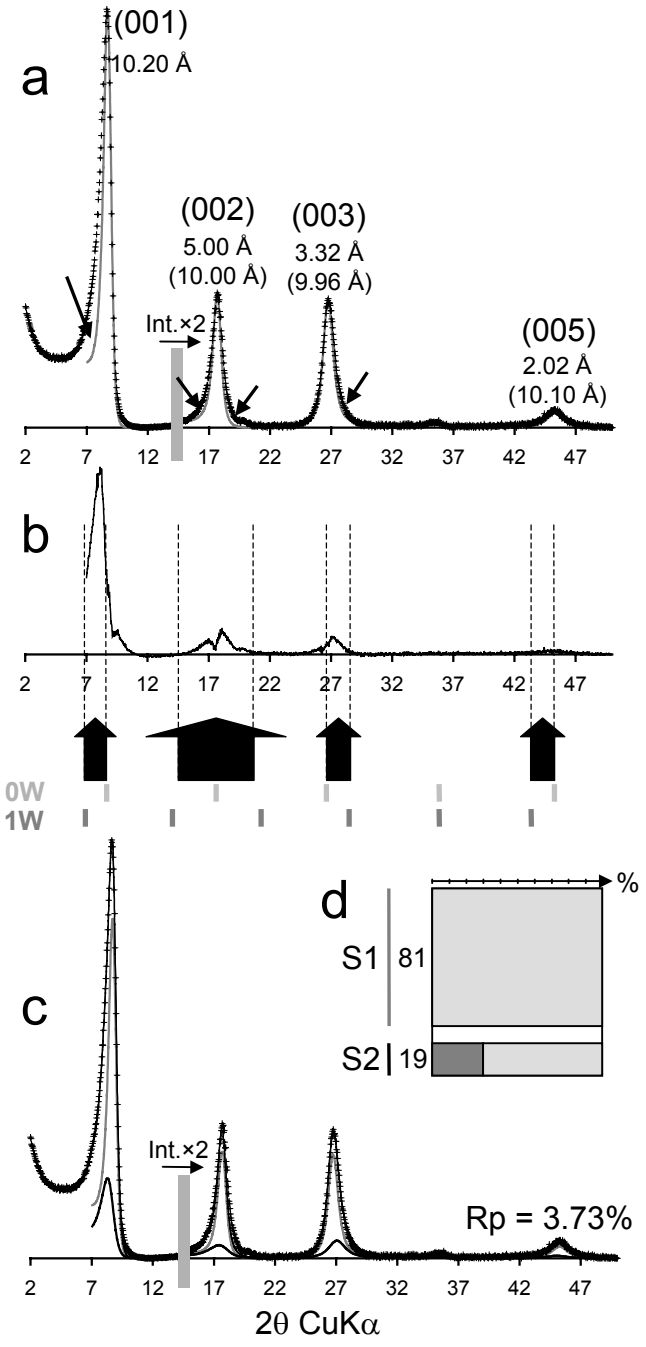

Ms#1776 Ferrage et al. Fig. 02

NEW VERSION

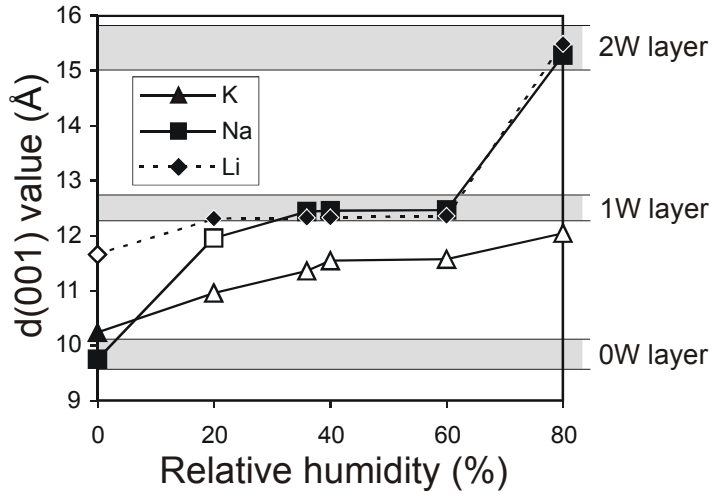

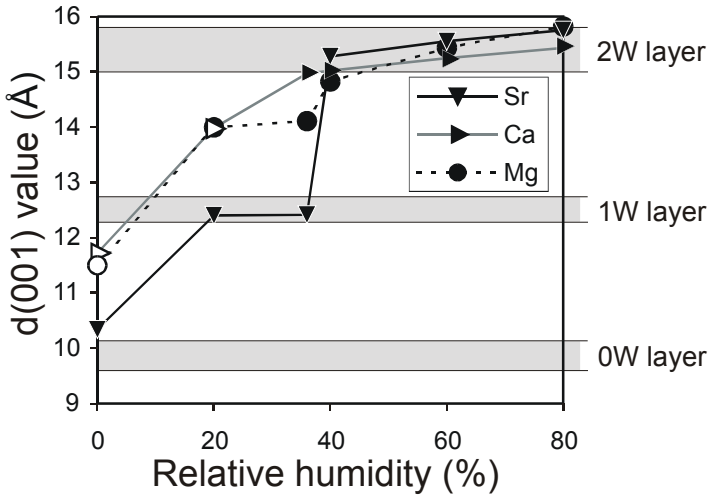

Ms#1776 Ferrage et al. Fig. 03

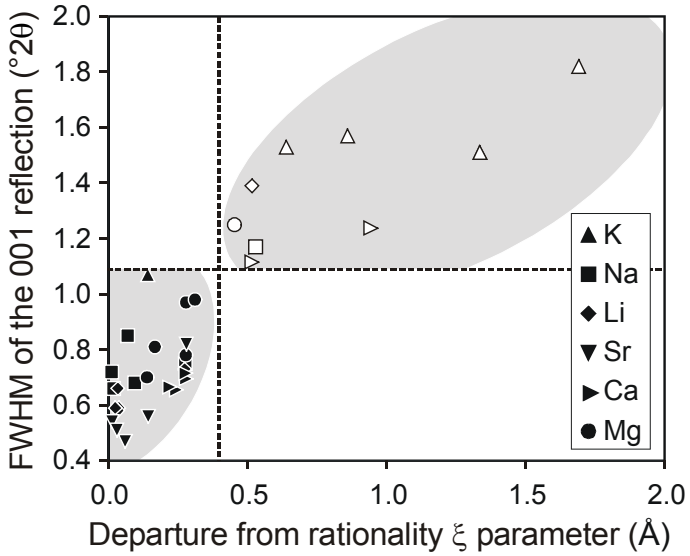

Ms#1776 Ferrage et al. Fig. 04

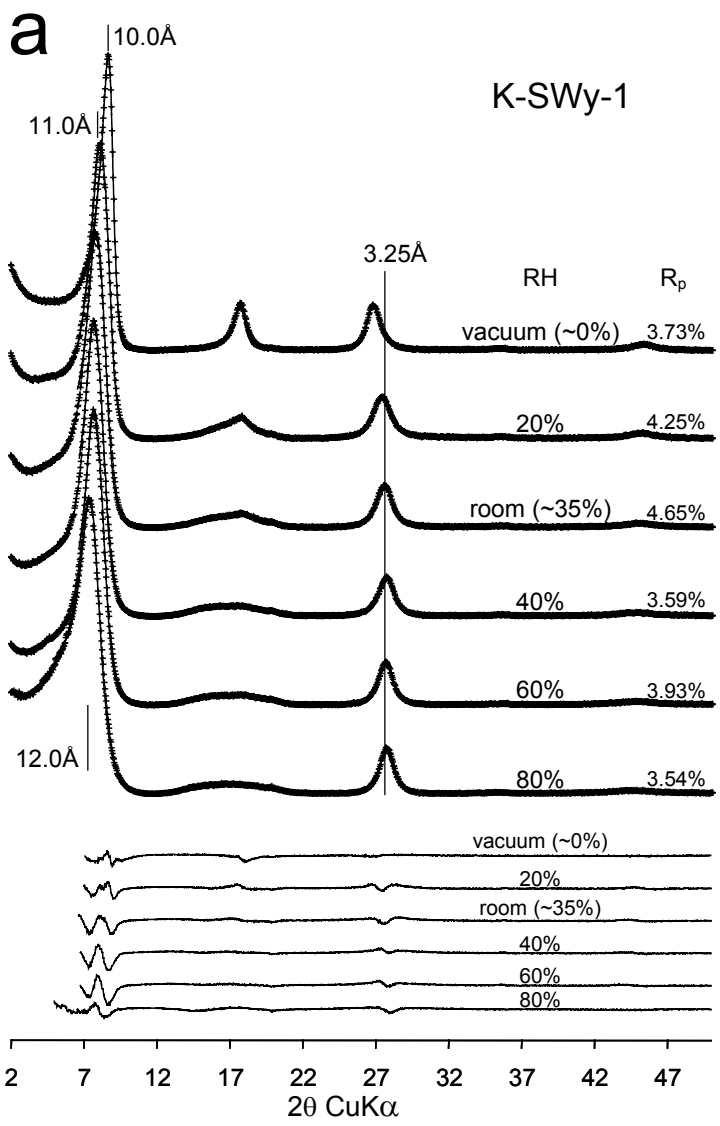

Ms#1776 Ferrage et al. Fig. 05a

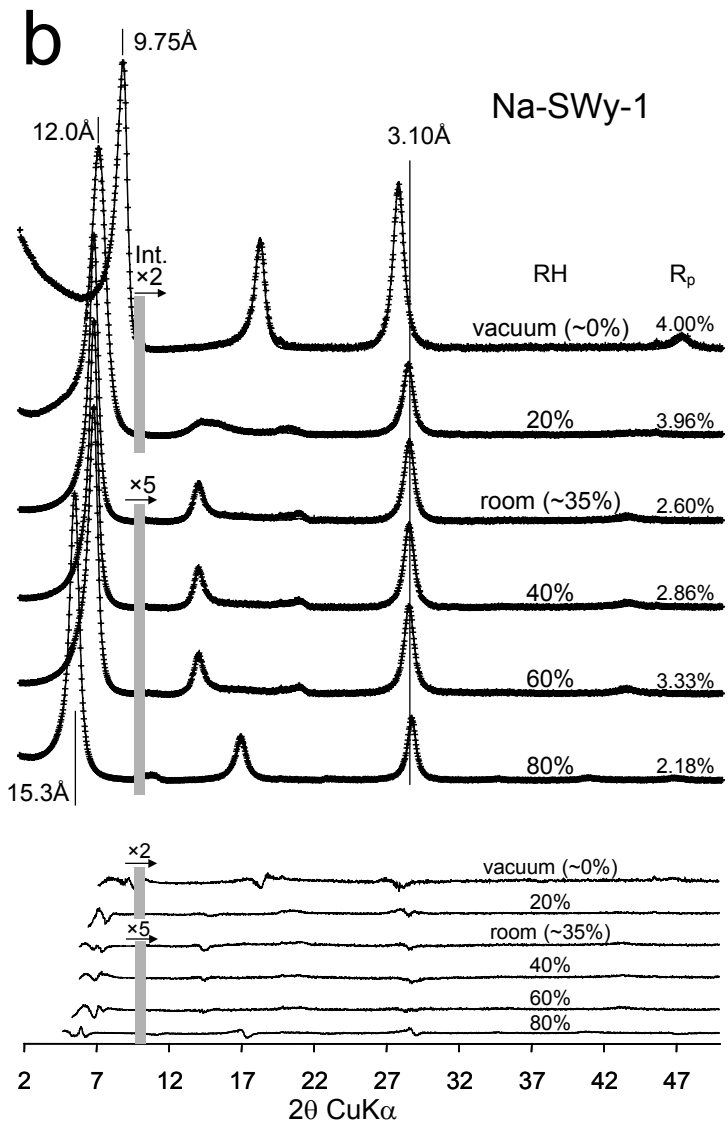

Ms#1776 Ferrage et al. Fig. 05b

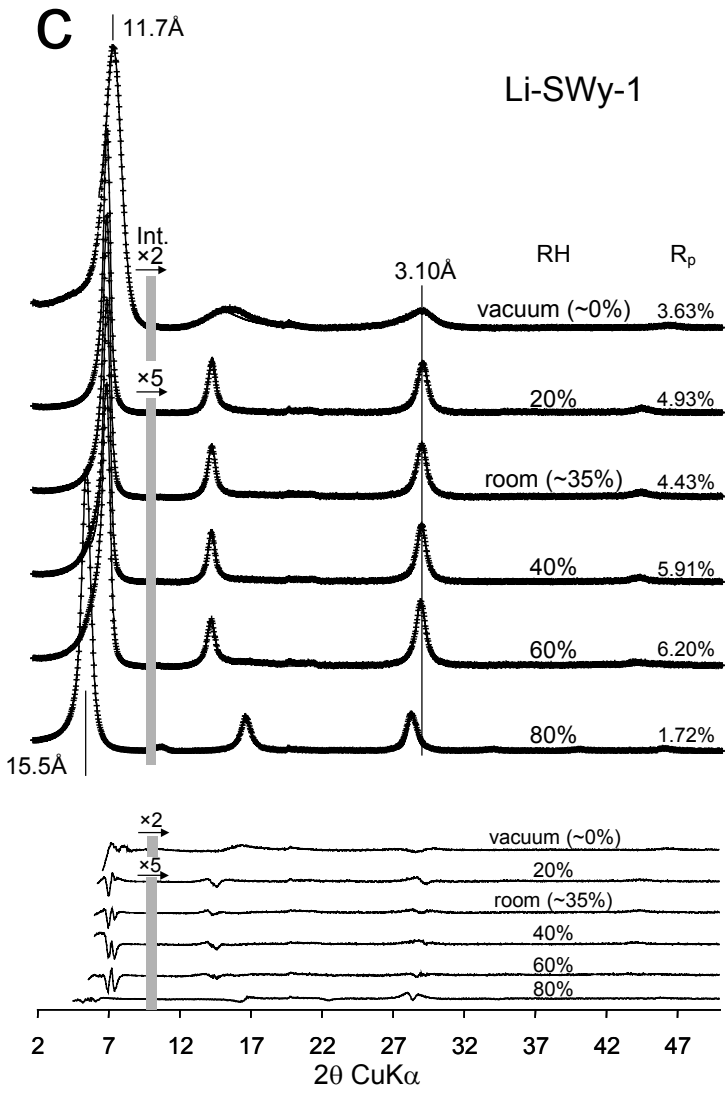

Ms#1776 Ferrage et al. Fig. 05c

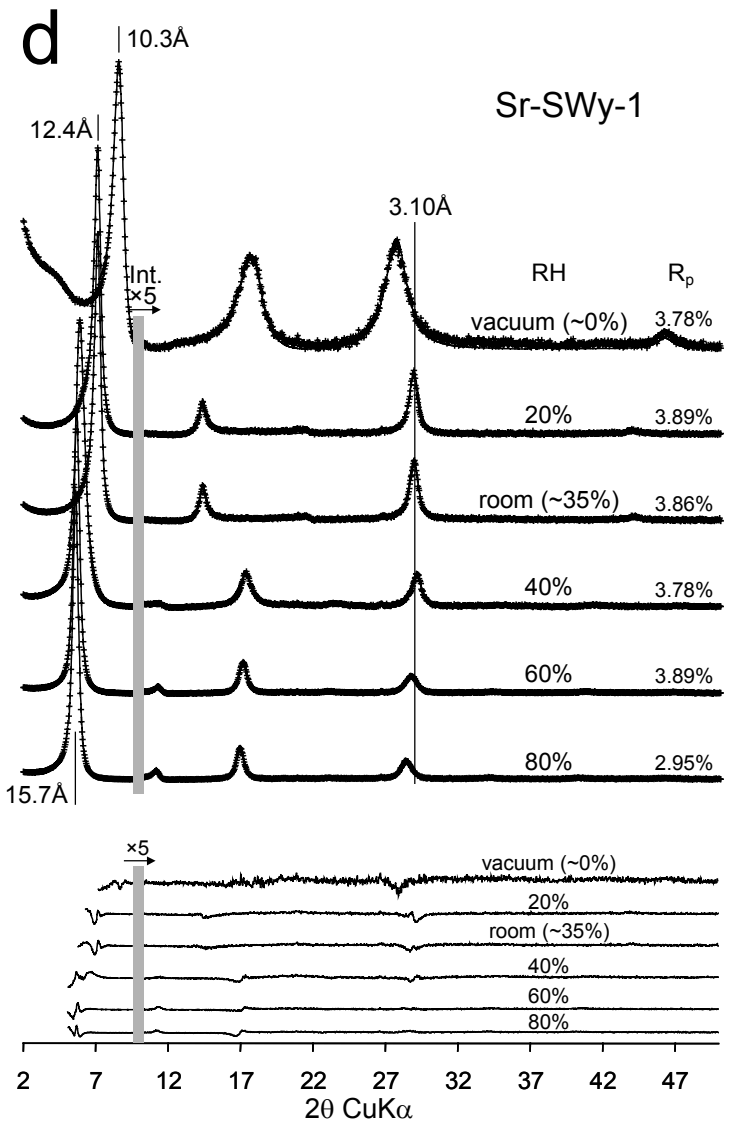

Ms#1776 Ferrage et al. Fig. 05d

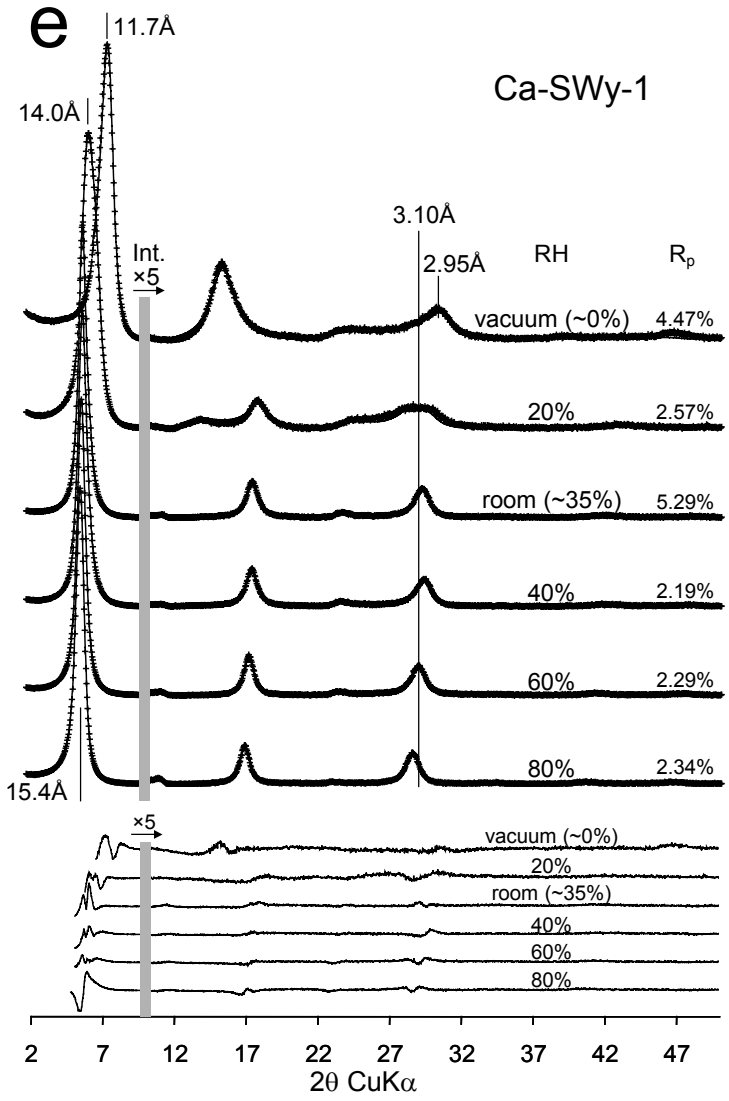

Ms#1776 Ferrage et al. Fig. 05e

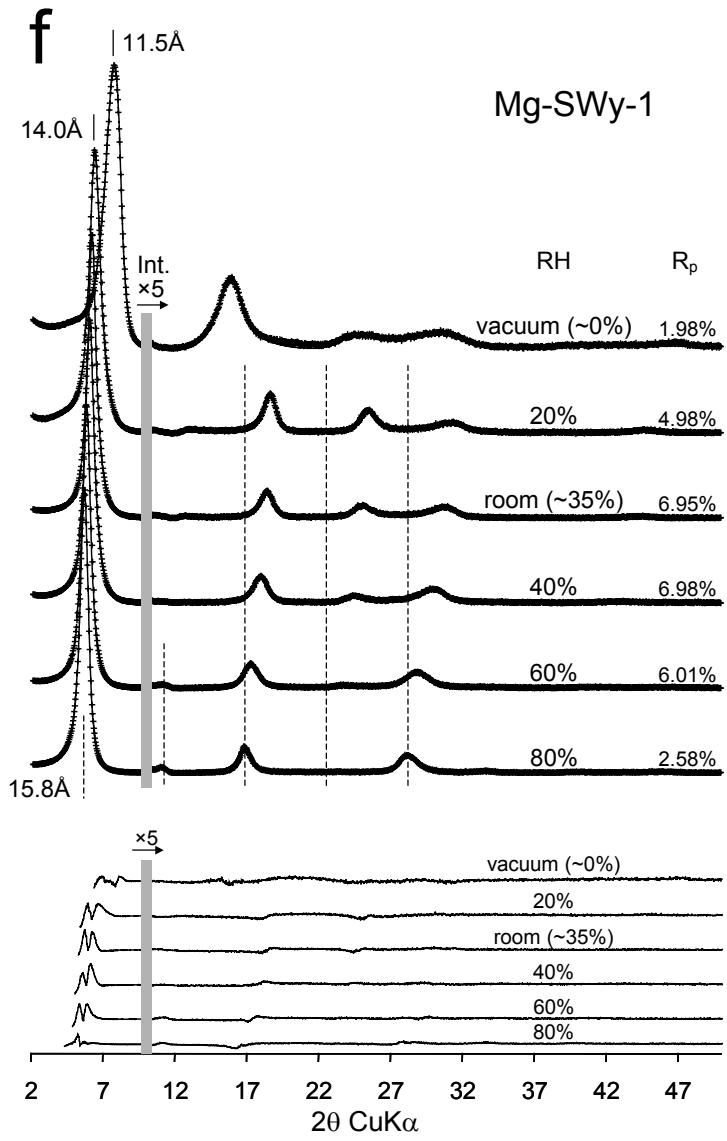

Ms#1776 Ferrage et al. Fig. 05f

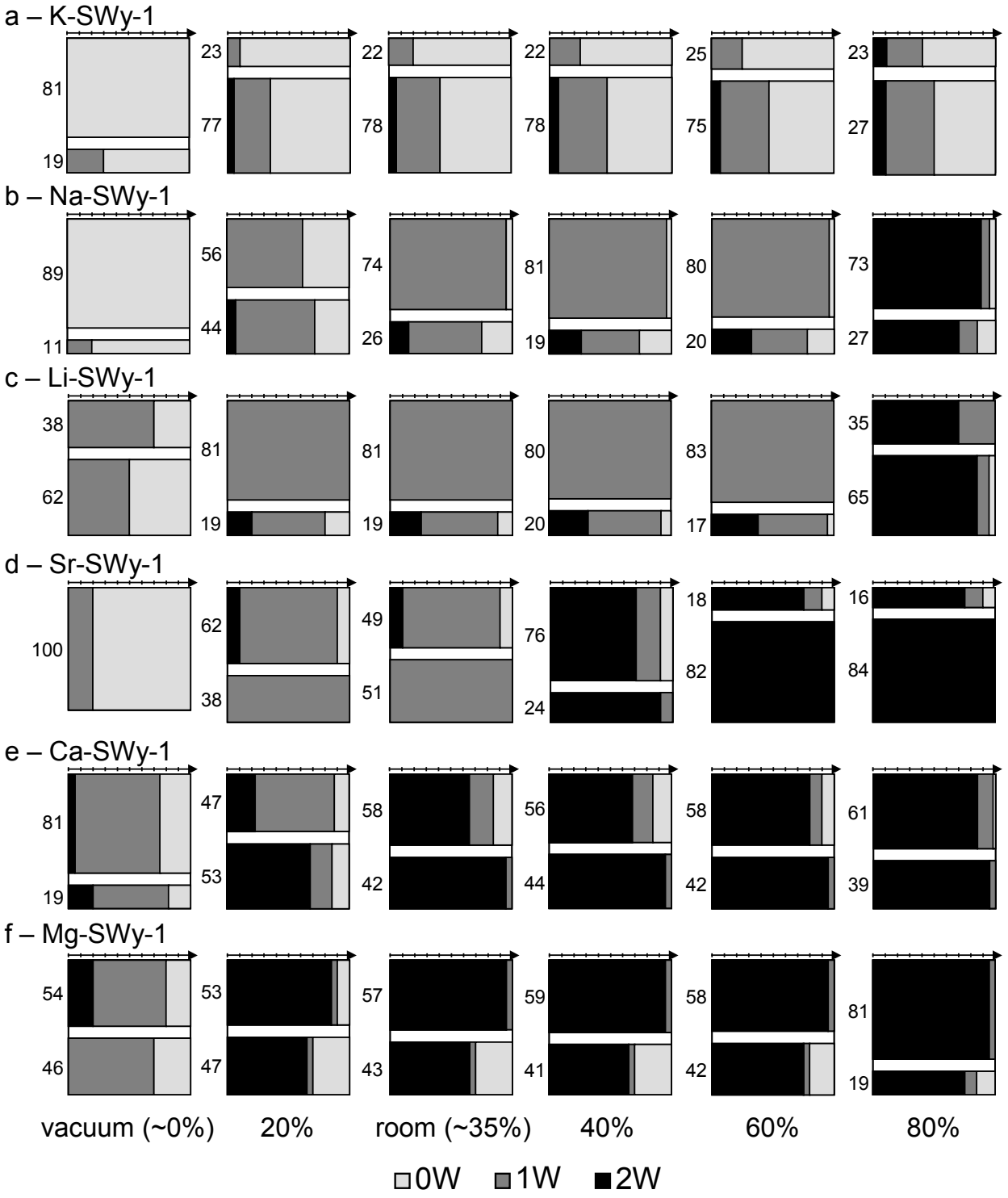

Please print in 2 columns format

Ms#1776 Ferrage et al. Fig. 06

NEW VERSION

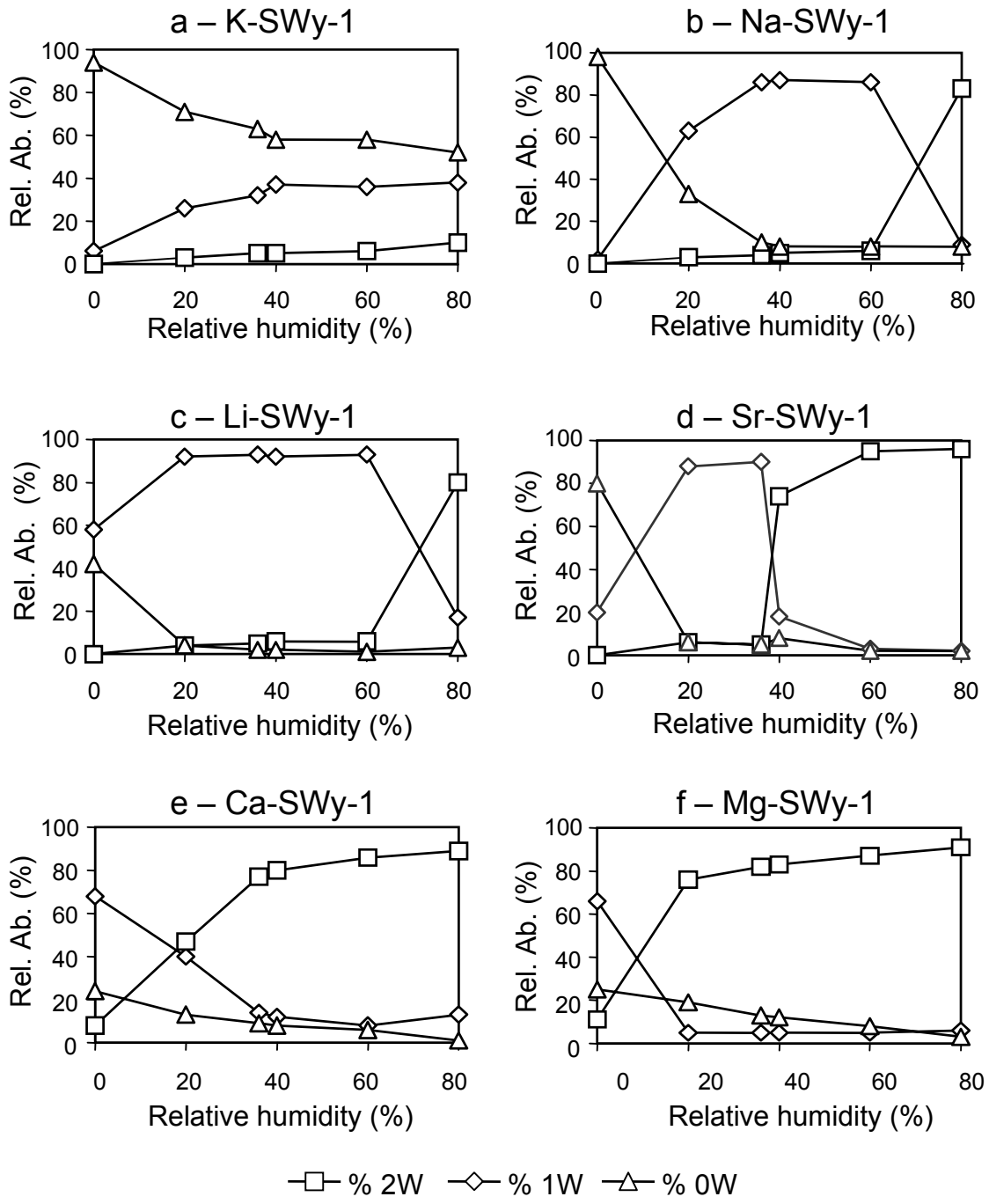

Please print in 2 column format

Ms#1776 Ferrage et al. Fig. 07

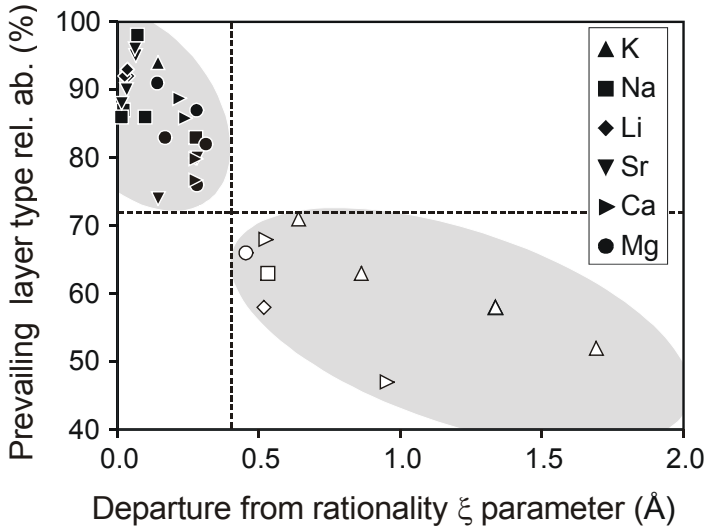

Ms#1776 Ferrage et al. Fig. 08

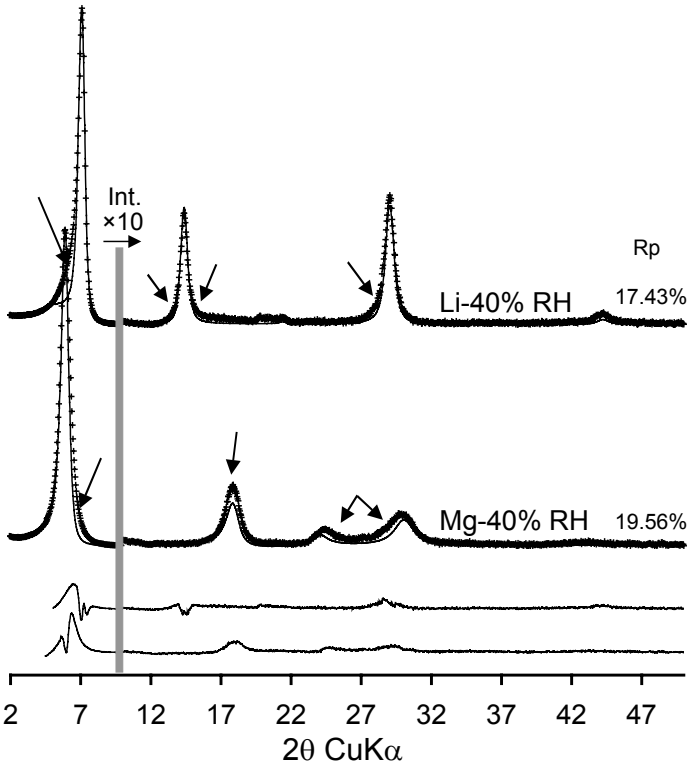

Ms#1776 Ferrage et al. Fig. 09

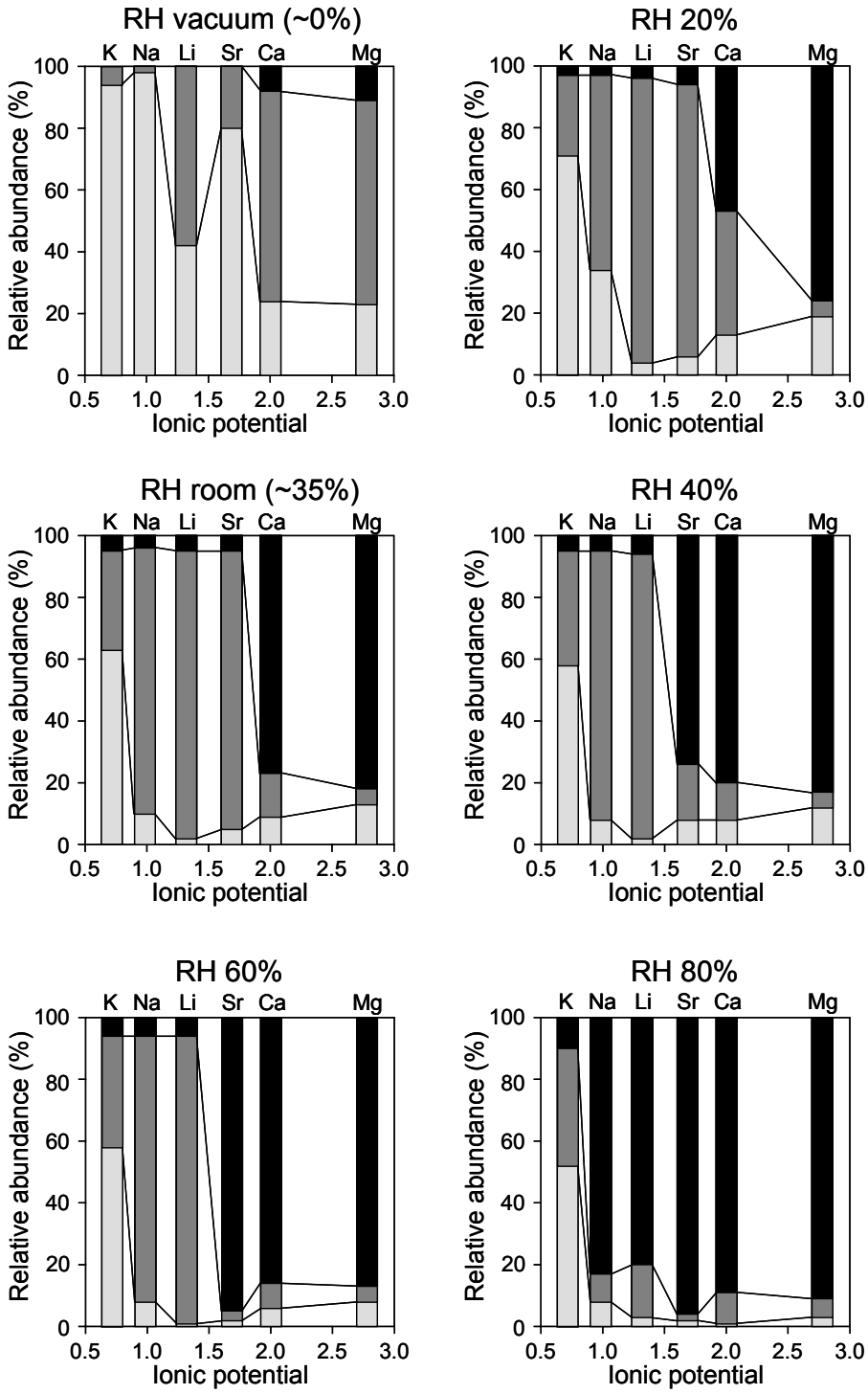

Please print in 2 column format

Ms#1776 Ferrage et al. Fig. 10

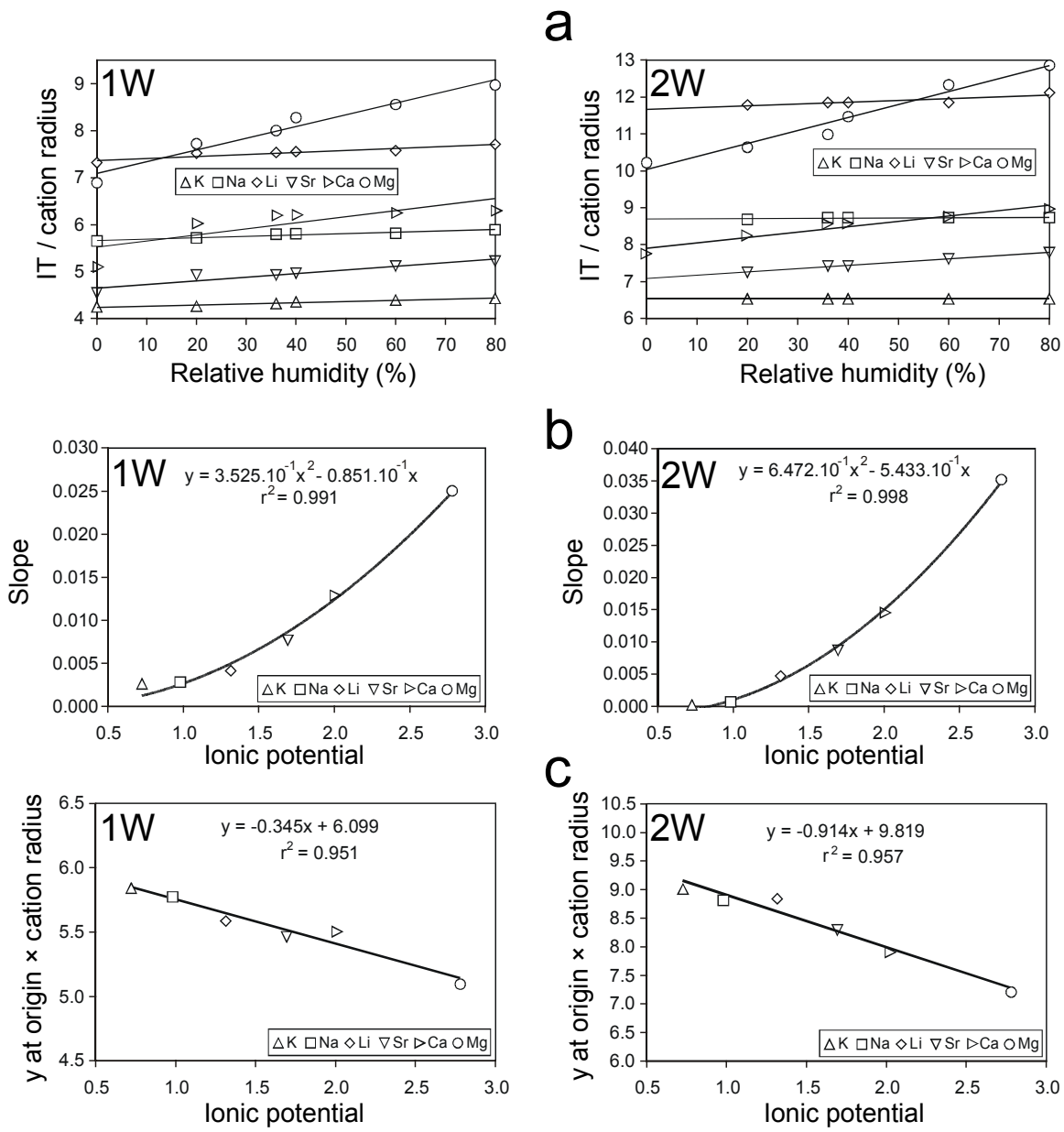

Please print in 2 column format

Ms#1776 Ferrage et al. Fig. 11

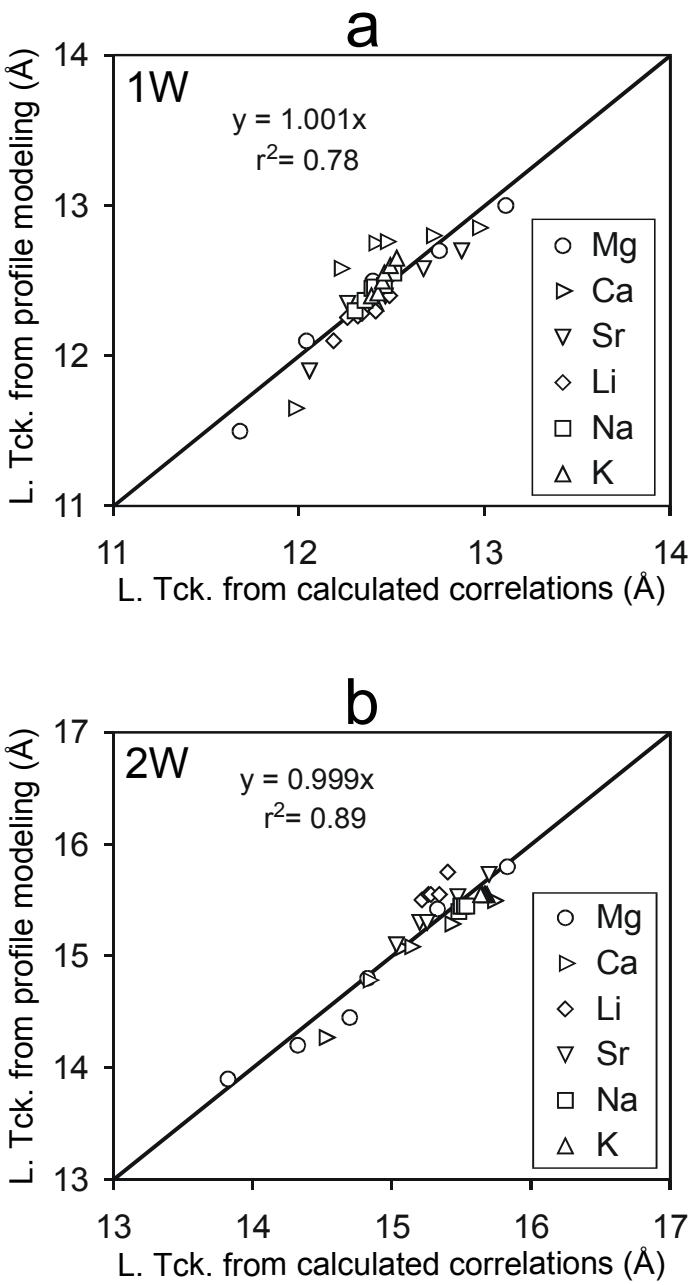

Ms#1776 Ferrage et al. Fig. 12

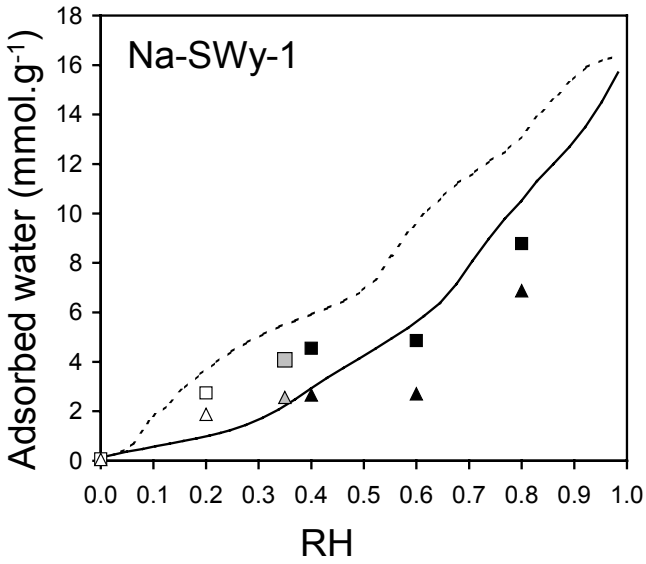

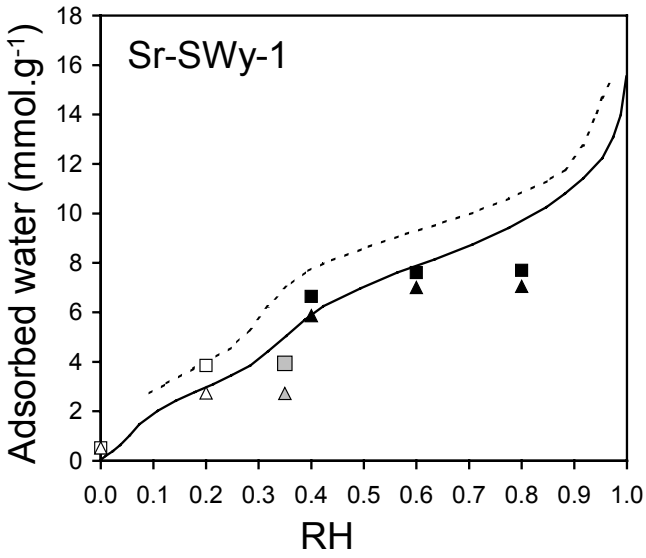

Ms#1776 Ferrage et al. Fig. 13

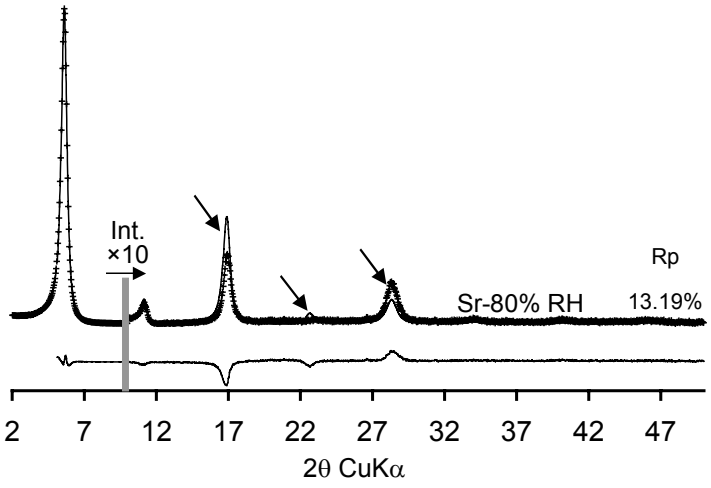

Ms#1776 Ferrage et al. Fig. 14